

Creation of Non-Abelian Topological Order and Anyons on a Trapped-Ion Processor

Mohsin Iqbal,^{1,*} Nathanan Tantivasadakarn,^{2,*} Ruben Verresen,^{3,*} Sara L. Campbell,⁴ Joan M. Dreiling,⁴ Caroline Figgatt,⁴ John P. Gaebler,⁴ Jacob Johansen,⁴ Michael Mills,⁴ Steven A. Moses,⁴ Juan M. Pino,⁴ Anthony Ransford,⁴ Mary Rowe,⁴ Peter Siegfried,⁴ Russell P. Stutz,⁴ Michael Foss-Feig,⁴ Ashvin Vishwanath,³ and Henrik Dreyer¹

¹Quantinuum, Leopoldstrasse 180, 80804 Munich, Germany

²Walter Burke Institute for Theoretical Physics and Department of Physics, California Institute of Technology, Pasadena, CA 91125, USA

³Department of Physics, Harvard University, Cambridge, MA 02138, USA

⁴Quantinuum, 303 S Technology Ct, Broomfield, CO 80021, USA

(Dated: May 9, 2023)

Non-Abelian topological order (TO) is a coveted state of matter with remarkable properties, including quasiparticles that can remember the sequence in which they are exchanged. These anyonic excitations are promising building blocks of fault-tolerant quantum computers. However, despite extensive efforts, non-Abelian TO and its excitations have remained elusive, unlike the simpler quasiparticles or defects in Abelian TO. In this work, we present the first unambiguous realization of non-Abelian TO and demonstrate control of its anyons. Using an adaptive circuit on Quantinuum’s H2 trapped-ion quantum processor, we create the ground state wavefunction of D_4 TO on a kagome lattice of 27 qubits, with fidelity per site exceeding 98.4%. By creating and moving anyons along Borromean rings in spacetime, anyon interferometry detects an intrinsically non-Abelian braiding process. Furthermore, tunneling non-Abelions around a torus creates all 22 ground states, as well as an excited state with a single anyon—a peculiar feature of non-Abelian TO. This work illustrates the counterintuitive nature of non-Abelions and enables their study in quantum devices.

I. INTRODUCTION

Wavefunctions can exhibit a type of entanglement called ‘topological order’, appearing at the frontiers of condensed matter and high-energy physics and forming the backbone of many proposals for fault-tolerant quantum information processing [1]. Such states come in two levels of complexity. The simplest topological wavefunctions are *Abelian*, whose pointlike excitations, called anyons, acquire a phase factor upon braiding one around another [2, 3] (see Fig. 1b). They have been proposed as robust quantum memories [4], and the fractional statistics of Abelian anyons have been verified in certain fractional quantum Hall states [5, 6]. More recently, the correlations associated to Abelian phases have been probed in a variety of engineered quantum devices [7–11].

The situation for *non-Abelian* topological phases is rather different [12–14]. These more exotic entangled states host excitations called non-Abelian anyons, which come with internal states. Braiding of non-Abelian particles generically effectuates a matrix action on this degenerate manifold. Such braiding is the operating principle of a topological quantum computer [15, 16]. This is associated to robustness to errors and thus defines a coveted goal, as is more generally the controlled realization of a non-Abelian topological phase—bringing their many remarkable properties under the experimental spotlight.

Thus far, however, the controlled preparation and braiding of anyons of a non-Abelian topological phase has evaded experiment. To date, the strongest candidate is the fractional quantum Hall state at $\nu = 5/2$

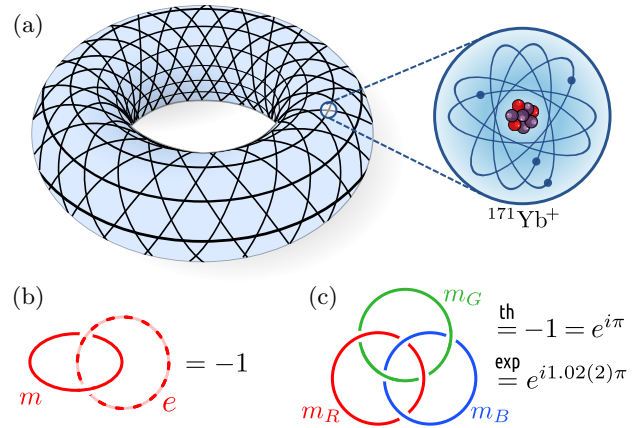


FIG. 1. **Creating and controlling non-Abelian wavefunctions.** (a) We entangle 27 ions to create the ground and excited states of a Hamiltonian with D_4 topological order on a kagome lattice with periodic boundary conditions. (b) Its excitations go beyond Abelian anyons, whose spacetime braiding depends only on pairwise linking, as exemplified by the e - and m -anyons of the toric code. (c) We create and control non-Abelian anyons $m_{R,G,B}$ which can detect Borromean ring braiding via anyon interferometry; see Fig. 5b of this work.

filling [17], which in numerical studies is identified with non-Abelian states. While thermal Hall measurements corroborate its non-Abelian nature by measuring a fractional chiral central charge c [18], the integer part of c from the same experiment differs from numerics and remains a puzzle [19]. Furthermore, there is currently no direct measurement of the non-Abelian statistics of excitations in this state. While anyons are pointlike, in other

* These authors contributed equally to this work.

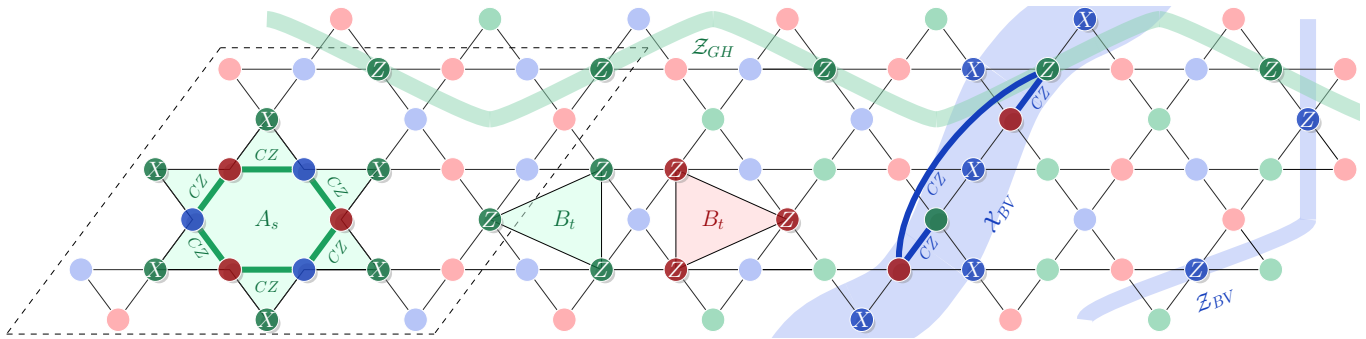


FIG. 2. **The non-Abelian D_4 model and its logical string operators.** We consider the model (1) on qubits that live on the vertices of a kagome lattice with periodic boundary conditions. Each kagome star is associated with three local operators: a 12-body star operator $A_s = \prod_{i=1}^6 CZ_{i,i+1} X^{\otimes 6}$ and two 3-body triangle operators $B_t = Z^{\otimes 3}$. It is convenient to choose a vertex coloring and assign a corresponding color to each of the qubits. For each of the three colors and direction along the torus, there are two logical string operators. The logical Z -operators are products of local Pauli- Z acting on all qubits of the respective colour in the chosen direction (Z_{GH} and Z_{BV} highlighted). For the logical X -operator (X_{BV} shown) a product of X is applied connecting stars of the the other two colors and decorated with a linear-depth circuit of CZ . More precisely, after choosing a starting point for the vertical string (here, bottom of figure) and direction (here, blue→red→green), we act with CZ gates connecting every green vertex with preceding red vertices on the path. In the experiment, we implement the system in the black dashed lines containing 3×3 stars (27 qubits) and periodic boundary conditions.

settings, the end points of line defects can display similar non-Abelian properties. Well-known examples are Majorana zero modes at the endpoints of $d = 1$ topological superconductors [20, 21] and lattice defects in $d = 2$ Abelian topological orders, such as in the toric code [22–24]. However, to the best of our knowledge, genuine non-Abelian topological order is a necessary condition for existing proposals for universal and topologically-protected quantum computation in two dimensions [15, 25–29].

In this work we realise non-Abelian topological order on Quantinuum’s H2 trapped-ion quantum processor. The effective all-to-all connectivity of the platform is used to create an entangled state of 27 ions with $D_4 \cong \mathbb{Z}_4 \rtimes \mathbb{Z}_2$ gauge symmetry (see Fig. 1a). We showcase increasingly exotic properties specific to non-Abelian topological order, including (i) a non-square ground state degeneracy of 22, (ii) braiding of non-Abelian anyons causing a non-trivial action on the ground state wavefunction, (iii) fusion of non-Abelian anyons that results in an excited state with a *single* anyon on the torus, and (iv) a non-trivial braiding sequence of three non-Abelions—also known as the “Borromean rings”—where the absence of pairwise linking makes it invisible to Abelions (Fig. 1b-c).

These experiments go beyond merely *simulating* non-Abelian order and statistics. The ions *are* entangled in precisely the same way as the low-energy states of Eq. (1), making them indistinguishable from states arising in the low-temperature limit of, e.g., a solid-state system governed by the same Hamiltonian. Ground state degeneracy then refers to the number of locally indistinguishable states, while anyons are local deformations which however cannot be individually created by a local process.

The ability to create such exotic entangled states owes to recent developments in experiment and theory. First, while it is known that topological order can only be pre-

pared with linear-depth unitary circuits [30, 31] limiting scalability, it has long been known that combining a finite-depth circuit of unitaries with measurement and feed-forward can prepare *Abelian* topological orders [32–35]. On the experimental side, it has only recently become possible to implement such adaptive circuits, illustrated by a toric code preparation [10, 11]. However, preparing *non-Abelian* states posed a challenge, since a straightforward extension of this procedure creates unpaired non-Abelions which require linear-depth unitaries to remove [36]. This efficient preparation problem was recently solved for a special class of ‘solvable’ non-Abelian topological orders [37–39], and was further simplified in the case of $\mathcal{D}(D_4)$ topological order in Ref. 40. This will be the strategy adopted in the current work.

II. THE MODEL

Our goal is to prepare and control eigenstates of a Hamiltonian of qubits arranged on the kagome lattice giving rise to non-Abelian topological order [41]:

$$H = - \sum_{s \in \{\star\}} A_s - \sum_{t \in \{\triangle, \triangleright\}} B_t. \quad (1)$$

The 12-body star operator $A_s = \prod_{i=1}^6 CZ_{i,i+1} X^{\otimes 6}$ and 3-body triangle operator $B_t = Z^{\otimes 3}$ are shown in Fig. 2. Note that each plaquette of the kagome lattice supports one A_s and two B_t terms. Moreover, we will take periodic boundary conditions, giving a toroidal geometry. It will be convenient to choose a three-coloring of the kagome lattice, which induces a coloring of each star and triangle term, as shown in Fig. 2; we will refer extensively to this red-green-blue coloring throughout the paper. While the

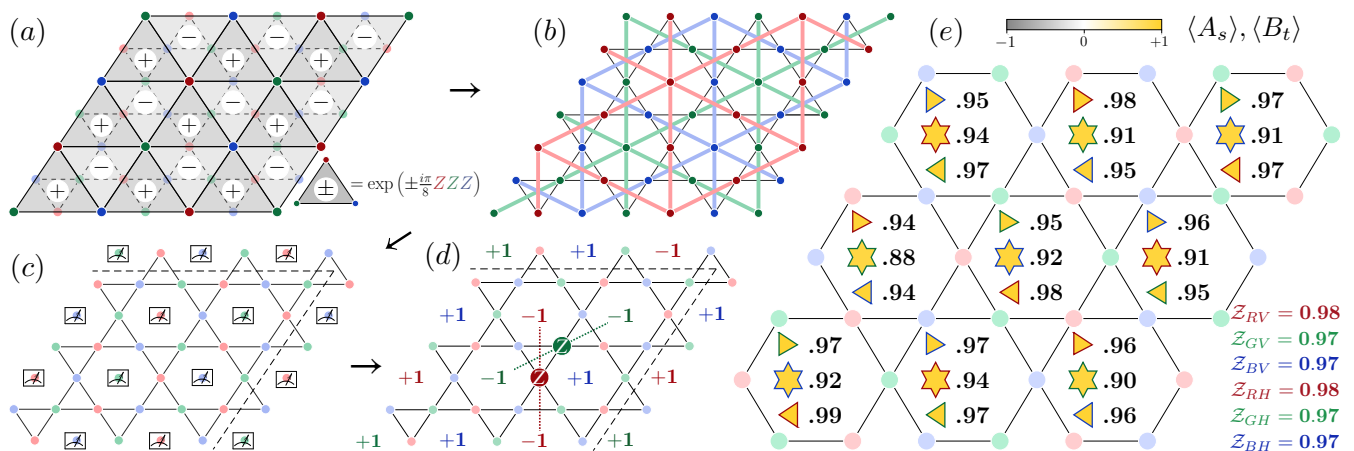


FIG. 3. **Ground state preparation protocol and experimental data.** (a) Starting with a $|+\rangle^{\otimes N_P}$ product state on the plaquettes of the kagome lattice, we entangle all qubits via non-Clifford three-qubit $\exp(\pm i\pi/8 ZZZ)$ gates; the sign in the exponent is +1 (−1) for up-pointing (down-pointing) triangles. On the device, pairs of adjacent three-qubit gates are compiled into four two-qubit gates (cf. section A 5). (b) The plaquette qubits are subsequently entangled with qubits living on the vertices of the kagome lattice (see Eq. (2)) via CNOT gates (colored lines). (c) Measuring the plaquette qubits in the X -basis prepares a state with non-Abelian topological order on the kagome lattice, albeit with a random pattern of Abelian anyons where the 12-body term $A_s = B_t = -1$. (d) A feed-forward layer of conditional Z gates is applied to pair up the Abelions, giving a state with $A_s = B_t = 1$. Dashed lines indicate the periodic boundary conditions. (e) After preparing the state, we experimentally measure the expectation values of star (A_s), triangle (B_t) and logical Z operators (see Fig. 2 for definitions). The measured energy density with respect to Eq. (1) is $-0.946(4)$. The average (maximal) standard error on the mean of the star and triangle operators is 0.015 (0.022). The average (maximal) standard error on logical operators is 0.004 (0.005).

Hamiltonian has been known for some time [41], below we present simple expressions for the anyon and logical operators which are essential for its experimental realization and verification.

Without the Controlled- Z gates in A_s , model (1) constitutes three decoupled toric code Hamiltonians [15] associated to (the bonds of) three triangular lattices in red, green and blue (Fig. 3b). The CZ gates couple the toric codes, leading to the A_s generally failing to commute with each other. Indeed, stabilizer Hamiltonians cannot support non-Abelian order [42]. Nevertheless, in the subspace where $B_t = 1$, we have $[A_s, A_{s'}] = 0$ and therefore all ground states fulfill $A_s = B_t = 1$. The violation of a star term $A_s = -1$ (triangle $B_t = -1$) signals the presence of an Abelian (a non-Abelian).

These states can be further distinguished by the value of logical string operators wrapping around the torus. Those operators act with Z on all qubits of a given color in either the horizontal or vertical direction (Fig. 2), and we will denote such operators by, e.g., Z_{RH} , with subscripts R, G, B denoting color and H, V denoting the horizontal or vertical direction. We first focus on the case where all Z -logicals are +1. Our last two sets of experiments explore the other logical sectors on the torus.

III. GROUND STATE PREPARATION

Our first goal is to prepare the unique ground state $|\psi_0\rangle$ of Eq. (1) with all logical Z -operators equal to +1. We employ a constant-depth adaptive circuit on the vertices

V of the kagome lattice proposed in Ref. 40, based on:

$$|\psi_0\rangle_V = \langle +|_P \prod_{\langle p,v \rangle} \text{CNOT}_{p,v} \prod_{\langle p,\tilde{p},\tilde{p} \rangle} e^{\pm \frac{i\pi}{8} Z_p Z_{\tilde{p}} Z_{\tilde{p}}} |+\rangle_P |0\rangle_V \quad (2)$$

where $\langle p,\tilde{p},\tilde{p} \rangle$ ranges over the triangular plaquettes of the ancillas P shown in Fig. 3a. Unpacking Eq. (2) into a preparation protocol, we start with a product state $|+\rangle_P |0\rangle_V$ which satisfies $B_t = Z = 1$. The protocol to also obtain $A_s = 1$ proceeds in three steps.

First, we entangle the ancillas $|+\rangle_P$ using the $\exp(\pm i\pi/8 ZZZ)$ -gates, giving a symmetry-protected topological (SPT) state with Z_3^2 symmetry [41, 43]. Subsequently, we entangle this SPT state to $|0\rangle_V$ by applying cluster state entanglers [44] on the three sublattices shown in Fig. 3b (up to a Hadamard transformation on V). Lastly, we measure all ancillas in the X -basis. If the outcome is +1, then Eq. (2) shows we obtain the desired state; this has been interpreted as effectively gauging the Z_3^2 symmetry of the SPT state [37] which indeed gives D_4 non-Abelian topological order (see Appendix A 4). If an outcome is −1, this signals the presence of an Abelian anyon on that star. These come in pairs for each color and applying appropriate Z -operators pair up the anyons at the end of the protocol (Fig. 3d). We stress that using such active feed-forward, we achieve deterministic state preparation without post-selection!

We implemented the above protocol for a kagome lattice containing 3×3 stars (27 qubits) on periodic boundary conditions. For this geometry, the ground state preparation naively requires $4N_{\text{stars}} = 36$ qubits and

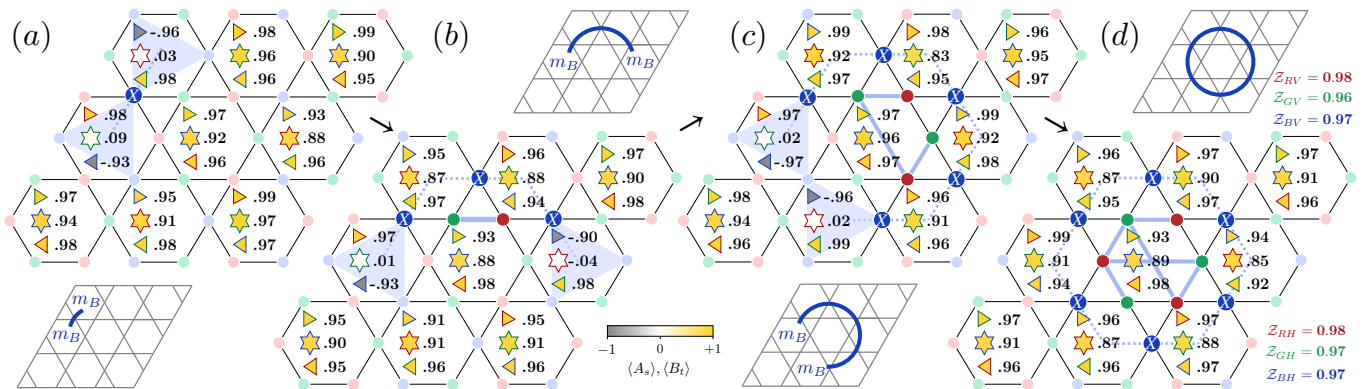


FIG. 4. **Creating and fusing a non-Abelian anyon pair.** (a) A non-Abelian pair is created from the vacuum by an X -operator that toggles the two adjacent blue triangles B_t (shaded). Exciting such a pair locally leads to $A_s = 0$ because pairs of star operators A_s anticommute if the product of triangles associated to the pair $B_t B_{t'} = -1$. Physically, this indeterminate value of A_s corresponds to the internal space of the non-Abelian. (b,c) Moving a non-Abelian requires a linear depth quantum circuit. To move a blue non-Abelian two stars over, we apply Pauli- X operators on blue qubits (blue dashed) and CZ operators between each red qubit and all preceding green qubits (thick blue). (d) Fusion of the blue non-Abelian pair in the identity channel brings the state back to $|\psi_0\rangle$. The average (maximum) standard error on the mean of star and triangle operators is 0.023 (0.068). The average (maximum) standard error on the mean of logical operators in (d) is 0.006 (0.008).

$12N_{\text{stars}} = 108$ two-qubit gates. Using circuit optimization and qubit reuse techniques, we reduce these requirements to 30 qubits and 78 two-qubit gates (cf. A 5). A barrier in the circuit ensures that the full state on 27 qubits is prepared before any measurement of the star, triangle, or logical operators. In practice, noise may corrupt the state in such a way that an odd number of star excitations is measured in step three of the protocol. These errors are heralded and we choose to discard the corresponding states leading to an average discard rate of 15% across all experiments reported (note that the scalability of the protocol is not affected [10]). After preparing the state, we measure the star, triangle and logical operators by executing single-qubit measurements in three different settings, each corresponding to one of the sublattices. The basis is chosen at the beginning of each shot.

The experimental results of this state preparation strategy are shown in Fig. 3e. Since $|\psi_0\rangle$ is completely specified by its star, triangle and logical expectation values, the data implies a bound of $\sqrt[27]{\langle \psi_0 | \rho_{\text{prepared}} | \psi_0 \rangle} \geq 0.984(1)$ on the fidelity per site for the raw data, and after correcting for readout error this increases to 0.990(1) giving a total fidelity of $\geq 0.75(2)$ (see section A 3 for a derivation). Remarkably, this fidelity per site is similar to a recent state-of-art constant-depth preparation of the much simpler toric code state [10].

IV. BRAIDING NON-ABELIAN ANYONS

Having established a high-fidelity state preparation protocol, we will now turn to the experimental exploration of the anyon content of the model. This phase of matter supports 22 anyons which are classified in Ap-

pendix A 4. We focus on three which are single-color non-Abelian bosons, denoted m_R , m_G and m_B , corresponding to violations of $B_t = 1$ (for a particular color).

While Abelian anyons can be moved using constant depth unitaries (and indeed we have employed such a layer of conditional Z -gates during the state preparation), separating a pair of non-Abelions necessarily requires a quantum circuit whose depth scales linearly with their distance [31, 36, 39]. In the present model, a pair of, e.g., m_B on two blue triangles t_i and t_f (one pointing left, one pointing right) can be created with the operator

$$X_{t_i}^{t_f} = \prod_b X_b \prod_{rg} CZ_{rg}. \quad (3)$$

where $\prod_{rg} CZ_{rg}$ is a linear-depth circuit of Controlled- Z 's. Its structure is such that, with the exception of the endpoints, we remain in the ground state (i.e., Eq. (3) commutes with all $B_{t \notin \{t_i, t_f\}}$, as well as all A_s in the $B_t = 1$ subspace). An example of such a string is shown in Fig. 2, where it defines the logical \mathcal{X} -operator upon wrapping around a periodic direction. Fig. 4 contains more examples, where we show experimental results for the creation, movement and annihilation of such a non-Abelian pair. This confirms the interpretation of triangle and star operators as indicators of the location of non-Abelions and Abelions, respectively. The results are compatible with the string leaving the state invariant away from its endpoint. The state is observed to return to the initial ground state after annihilating the pair.

The above process can be interpreted in terms of the fusion rules of the model. Specifically, for the anyons considered,

$$m_B \times m_B = 1 + e_R + e_G + e_R e_G \quad (4)$$

where e_R and e_G are Abelian bosons corresponding to

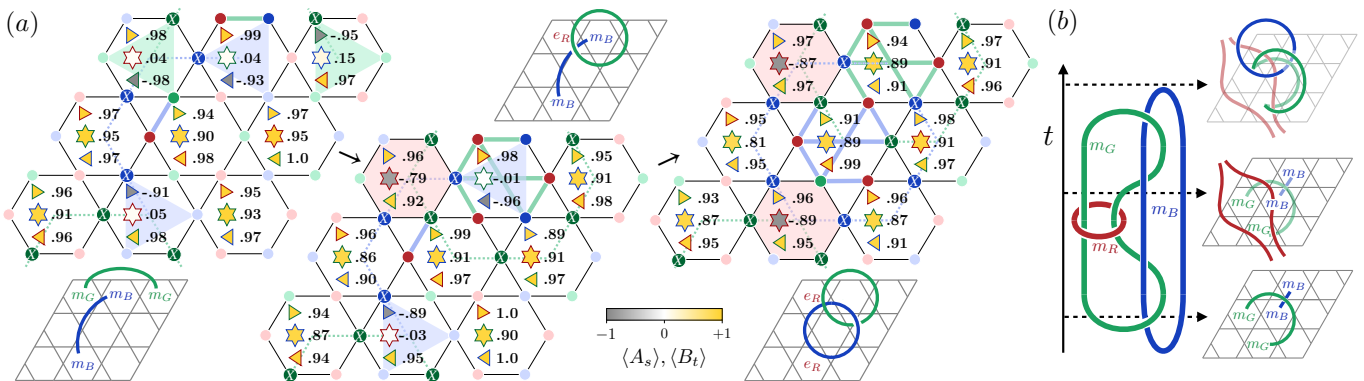


FIG. 5. **Braiding non-Abelian anyons.** (a) A pair of blue non-Abelian fluxes m_B is created, indicated by excited triangle operators. Subsequently, one partner of a pair of green m_G is braided around one of the m_B and annihilated, leaving behind an e_R (shaded) due to the fusion rules (4). The upper blue anyon is then brought back to its partner, creating another e_R . The average (maximum) standard error on the mean of star and triangle operators is 0.025 (0.069). (b) Borromean braiding in spacetime. Pairs of m_B , m_G and m_R are created and braided in such a way that each pair is unlinked. Thumbnails show the operators applied at different points in time. The creation and movement of the the m_B is controlled on an ancilla, allowing to extract the phase $1.02(2)\pi$. For Abelian anyons the phase of the corresponding diagram would be 0 (see Fig. 1).

$A_s = -1$. The fusion channel of a single m_B -pair created from the vacuum is necessarily the identity ‘1’. In a topological quantum computer, the fusion channel is the degree of freedom that encodes the quantum information. The ability to change the internal state of the non-Abelions is a necessary requirement for topological quantum computation. Demonstrating this ability is what we turn to next.

Specifically, braiding m_G around m_B toggles the fusion channel for both pairs from 1 to e_R , essentially executing a Pauli- X -gate on the fusion channel space. The results of this braiding are reported in Fig. 5a. After the annihilation of both pairs, the state is found to be in the ground state, except at the points where m_B and m_G were annihilated. There, negative values of the star operators indicate the presence of e_R -Abelions. The fusion product is not visible during the braiding process but only reveals itself upon annihilation of the anyons, evidencing the fact that information is stored non-locally in the entanglement of the wavefunction.

Even when there is no net linking between non-Abelian worldlines—such that we fuse back to the vacuum at the end—the non-Abelian fusion rules can lead to striking consequences. In particular, we can detect a three-anyon braiding which would be invisible for a purely Abelian state. Concretely, pairs of m_R , m_G and m_B are created, moved and annihilated in such a way to form “Borromean rings” in spacetime (Fig. 5b) [45–47]. The defining property of this linking is that any pair of rings is unlinked such that the removal of any one of them renders the diagram topologically trivial. Thus, for any triplet of Abelian particles, such a braiding action must necessarily be trivial (cf. Fig. 1). In stark contrast, in the present model, the ground state is theoretically predicted to pick up a minus sign under a Borromean braid. We have implemented a Hadamard test to obtain the braiding phase,

confirming experimentally the phase

$$\arg \langle \psi_0 | X_g' X_r^r X_g^g X_b^b X_g^g X_r^r X_g' X_b^b | \psi_0 \rangle = 1.02(2)\pi$$

(see Fig. 5b and Extended Data Figure 10 for the microscopic definition of the operators). Removing the red or green action trivialises the action and we find phases of $0.00(2)\pi$ and $0.07(2)\pi$ for those braids, respectively.

V. LOGICAL SECTORS AND SINGLE ANYONS

Thus far, our experiments have created ground states and anyons in the logical $\mathcal{Z} = +1$ -sector of the D_4 model. We can toggle between the logical- \mathcal{Z} eigenstates by moving m anyons around the torus. An example of such a logical- \mathcal{X}_{BV} operator, which toggles \mathcal{Z}_{BH} , is shown in Fig. 2. As we now show, the non-Abelian nature of these anyons leads to striking consequences for these different sectors.

In principle, there are $2^6 = 64$ different assignments of ± 1 to the six logical \mathcal{Z} -operators. However, in stark contrast to Abelian topological orders (like the toric code), there is a non-trivial constraint

$$\prod_{s \in \{\star\}} A_s = (-1)^{\frac{1-\mathcal{Z}_{GH}}{2} \frac{1-\mathcal{Z}_{BV}}{2}} \times (-1)^{\frac{1-\mathcal{Z}_{GV}}{2} \frac{1-\mathcal{Z}_{BH}}{2}} \quad (5)$$

between the star and logical operators in the $B_t = 1$ subspace and analogous relations holds for the other colours (see Appendix A2 for a derivation). To keep the right-hand side of Eq. (5) positive, we can apply any combination of horizontal $\mathcal{X}_{\lambda H}$ -logicals, or vertical $\mathcal{X}_{\lambda V}$ -logicals, or $\mathcal{X}_{\lambda H} \mathcal{X}_{\lambda V}$ -logicals. This leads to a degeneracy of $1 + (2^3 - 1) \times 3 = 22$ ground states with $A_s = B_t = +1$. It can be shown that there are no other ground states (see Appendix A2). We have experimentally created all

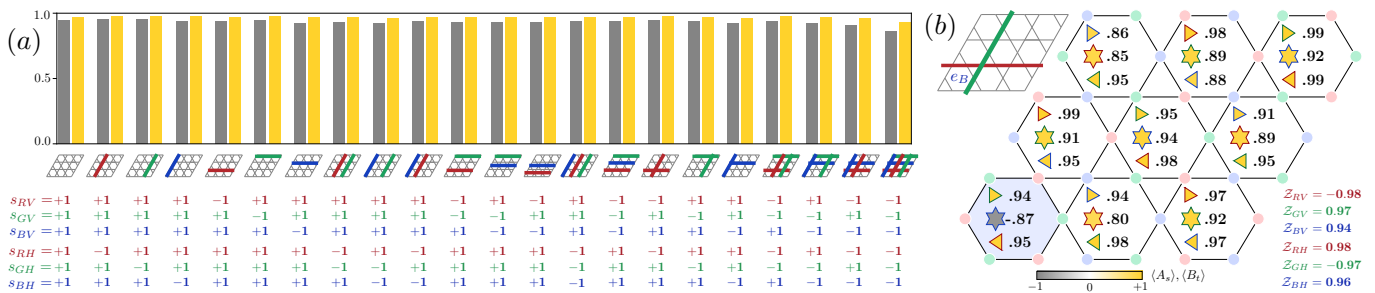


FIG. 6. **Creation of all 22 ground states and a state with a single anyon on the torus.** (a) Logical \mathcal{X} -operators are applied by winding non-Abelian anyons around the torus. There are $2^6 = 64$ possible combinations, the 22 configurations shown here fulfill the constraint $A_s = 1$ for each color according to (5). The bar plot shows experimentally measured values of the negative energy density (gray) and a logical pinning function (yellow) $\Pi := 1/6 \sum_{cd} s_{cd} \overline{\mathcal{Z}_{cd}}$ where c and d run over the three colors and two directions, respectively, $\overline{\mathcal{Z}_{cd}}$ is the corresponding logical \mathcal{Z} operator averaged over translations and $s_{cd} = \pm 1$ is the sign of \mathcal{Z}_{cd} in the target logical sector. This operator is equal to 1 if and only if the state is in the theoretically predicted logical sector. All of the 22 states are found to be ground states in distinct logical sectors. The average of the energy density (logical pinning function) across 22 ground states is -0.93 (0.97). The average (maximum) standard error on the mean of the energy densities and logical pinning functions is 0.007 (0.009) and 0.003 (0.004), respectively. (b) A red horizontal and green vertical \mathcal{X} operator are applied to the ground state. The red non-Abelian flips the logical \mathcal{Z} operator that toggles the fusion channel of the green pair. The state after this procedure is experimentally found to have a single blue Abelian excitation. The average (maximum) standard error on the mean of the energy and logicals is 0.017 (0.029) and 0.005 (0.007), respectively.

22 states by applying the above logical- \mathcal{X} operators to our initial $|\psi_0\rangle$. The main results are shown in Fig. 6a, with a full set of expectation values reported in Extended Data Table III. We have thus demonstrated the control necessary to experimentally access the full ground state subspace.

The existence of a ground state degeneracy that is not a perfect square is a striking consequence of the non-Abelian order. This is further emphasized by considering the fate of logical sectors where the right-hand side of Eq. (5) is negative. Apparently, such states host an *odd* number of Abelian anyons. We experimentally confirm this curious prediction by applying $\mathcal{X}_{GV}\mathcal{X}_{RH}$ to $|\psi_0\rangle$. Strikingly, we measure a *single* anyon e_B in the resulting state (Fig. 6b)!

VI. OUTLOOK

In this work we have demonstrated the creation of ground states with non-Abelian topological order as well as the controlled braiding of non-Abelian anyons and tunneling between logical states on a trapped-ion quantum processor. Our key finding is that non-Abelian topological orders can experimentally be prepared with high fidelities on par with Abelian states like the surface code. Non-Abelian states are among the most intricately entangled quantum states theoretically known to exist, and carry promises for new types of quantum information

processing. The fact that these states can now be faithfully prepared and controlled is a testimony to the rapid development of quantum devices over the last decade and opens up several new questions.

Unlike ground states of Abelian topological order, logical states in the D_4 -model can only be toggled via a linear-depth circuit. Whether this property leads to a greater tolerance against bit-flip noise is an interesting question to explore. Moreover, rather than utilizing energy conservation to protect our state, we envisage stabilizing it by repeatedly measuring the terms in Eq. (1) and pairing up the anyons using the above string operators. A fault-tolerant threshold for D_4 topological order has been argued for [48], and a deeper exploration of these issues is left to future work.

More broadly, it would be fascinating to create and explore other novel types of entangled phases of matter. Certain ‘solvable’ non-Abelian states can be accessed by utilizing multiple rounds of measurement [35, 37–39], whereas others can be obtained from log-depth adaptive circuits [49]. Remarkably, finite-depth adaptive circuits have even been proposed to create states with algebraic correlations [50–52].

Finally, it is not known whether the gate set implemented by measurement and braiding of anyons with D_4 order can be made universal. However, universal S_3 states [25, 53] can be created by adding a single layer of feed-forward [35]. Our work thus points a way toward demonstrating the first universal gate set from braiding non-Abelions and measurement.

[1] X.-G. Wen, *Quantum field theory of many-body systems*, Oxford Graduate Texts (Oxford University Press, Ox-

ford, 2010).

- [2] J. M. Leinaas and J. Myrheim, On the theory of identical particles, *Il Nuovo Cimento B (1971-1996)* **37**, 1 (1977).
- [3] F. Wilczek, Quantum Mechanics of Fractional-Spin Particles, *Physical Review Letters* **49**, 957 (1982).
- [4] A. G. Fowler, M. Mariantoni, J. M. Martinis, and A. N. Cleland, Surface codes: Towards practical large-scale quantum computation, *Physical Review A* **86**, 032324 (2012).
- [5] J. Nakamura, S. Liang, G. C. Gardner, and M. J. Manfra, Direct observation of anyonic braiding statistics, *Nature Physics* **16**, 931 (2020).
- [6] H. Bartolomei, M. Kumar, R. Bisognin, A. Marguerite, J.-M. Berroir, E. Bocquillon, B. Plaças, A. Cavanna, Q. Dong, U. Gennser, Y. Jin, and G. Fève, Fractional statistics in anyon collisions, *Science* **368**, 173 (2020).
- [7] K. J. Satzinger, Y. Liu, A. Smith, C. Knapp, M. Newman, C. Jones, Z. Chen, C. Quintana, X. Mi, A. Dunsworth, C. Gidney, I. Aleiner, F. Arute, K. Arya, J. Atalaya, R. Babbush, J. C. Bardin, R. Barends, J. Basso, A. Bengtsson, A. Bilmes, M. Broughton, B. B. Buckley, D. A. Buell, B. Burkett, N. Bushnell, B. Chiaro, R. Collins, W. Courtney, S. Demura, A. R. Derk, D. Eppens, C. Erickson, E. Farhi, L. Foaro, A. G. Fowler, B. Foxen, M. Giustina, A. Greene, J. A. Gross, M. P. Harrigan, S. D. Harrington, J. Hilton, S. Hong, T. Huang, W. J. Huggins, L. B. Ioffe, S. V. Isakov, E. Jeffrey, Z. Jiang, D. Kafri, K. Kechedzhi, T. Khattar, S. Kim, P. V. Klimov, A. N. Korotkov, F. Kostritsa, D. Landhuis, P. Laptev, A. Locharla, E. Lucero, O. Martin, J. R. McClean, M. McEwen, K. C. Miao, M. Mohseni, S. Montazeri, W. Mruczkiewicz, J. Mutus, O. Naaman, M. Neeley, C. Neill, M. Y. Niu, T. E. O'Brien, A. Opremcak, B. Pató, A. Petukhov, N. C. Rubin, D. Sank, V. Shvarts, D. Strain, M. Szalay, B. Villalonga, T. C. White, Z. Yao, P. Yeh, J. Yoo, A. Zalcman, H. Neven, S. Boixo, A. Megrant, Y. Chen, J. Kelly, V. Smelyanskiy, A. Kitaev, M. Knap, F. Pollmann, and P. Roushan, Realizing topologically ordered states on a quantum processor, *Science* **374**, 1237 (2021).
- [8] G. Semeghini, H. Levine, A. Keesling, S. Ebadi, T. T. Wang, D. Bluvstein, R. Verresen, H. Pichler, M. Kalinowski, R. Samajdar, A. Omran, S. Sachdev, A. Vishwanath, M. Greiner, V. Vuletić, and M. D. Lukin, Probing topological spin liquids on a programmable quantum simulator, *Science* **374**, 1242 (2021).
- [9] C. Ryan-Anderson, N. C. Brown, M. S. Allman, B. Arkin, G. Asa-Attuah, C. Baldwin, J. Berg, J. G. Bohnet, S. Braxton, N. Burdick, J. P. Campora, A. Chernoguzov, J. Esposito, B. Evans, D. Francois, J. P. Gaebler, T. M. Gatterman, J. Gerber, K. Gilmore, D. Gresh, A. Hall, A. Hankin, J. Hostetter, D. Lucchetti, K. Mayer, J. Myers, B. Neyenhuis, J. Santiago, J. Sedlacek, T. Skripka, A. Slattey, R. P. Stutz, J. Tait, R. Tobey, G. Vittorini, J. Walker, and D. Hayes, [Implementing Fault-tolerant Entangling Gates on the Five-qubit Code and the Color Code](#) (2022).
- [10] M. Iqbal, N. Tantivasadakarn, T. M. Gatterman, J. A. Gerber, K. Gilmore, D. Gresh, A. Hankin, N. Hewitt, C. V. Horst, M. Matheny, T. Mengle, B. Neyenhuis, A. Vishwanath, M. Foss-Feig, R. Verresen, and H. Dreyer, [Topological Order from Measurements and Feed-Forward on a Trapped Ion Quantum Computer](#) (2023).
- [11] M. Foss-Feig, A. Tikku, T.-C. Lu, K. Mayer, M. Iqbal, T. M. Gatterman, J. A. Gerber, K. Gilmore, D. Gresh, A. Hankin, N. Hewitt, C. V. Horst, M. Matheny, T. Mengle, B. Neyenhuis, H. Dreyer, D. Hayes, T. H. Hsieh, and I. H. Kim, Experimental demonstration of the advantage of adaptive quantum circuits (2023), [arXiv:2302.03029 \[quant-ph\]](#).
- [12] E. Witten, Quantum field theory and the Jones polynomial, *Communications in Mathematical Physics* **121**, 351 (1989).
- [13] G. Moore and N. Seiberg, Classical and quantum conformal field theory, *Communications in Mathematical Physics* **123**, 177 (1989).
- [14] G. Moore and N. Read, Nonabelions in the fractional quantum hall effect, *Nuclear Physics B* **360**, 362 (1991).
- [15] A. Y. Kitaev, Fault-tolerant quantum computation by anyons, *Annals of Physics* **303**, 2 (2003).
- [16] C. Nayak, S. H. Simon, A. Stern, M. Freedman, and S. Das Sarma, Non-Abelian anyons and topological quantum computation, *Reviews of Modern Physics* **80**, 1083 (2008).
- [17] W. Pan, J.-S. Xia, V. Shvarts, E. D. Adams, H. L. Stormer, D. C. Tsui, L. N. Pfeiffer, K. W. Baldwin, and K. W. West, Exact Quantization of Even-Denominator Fractional Quantum Hall State at $\nu=5/2$ Landau Level Filling Factor, *Physical Review Letters* **83**, 3530 (1999), [arXiv:cond-mat/9907356](#).
- [18] M. Banerjee, M. Heiblum, V. Umansky, D. E. Feldman, Y. Oreg, and A. Stern, Observation of half-integer thermal Hall conductance, *Nature* **559**, 205 (2018).
- [19] K. K. W. Ma, M. R. Peterson, V. W. Scarola, and K. Yang, [Fractional quantum Hall effect at the filling factor \$\nu=5/2\$](#) (2022).
- [20] A. Kitaev, Unpaired Majorana fermions in quantum wires, *Physics-Uspekhi* **44**, 131 (2001).
- [21] M. Aghaee, A. Akkala, Z. Alam, R. Ali, A. A. Ramirez, M. Andrzejczuk, A. E. Antipov, P. Aseev, M. Astafev, B. Bauer, J. Becker, S. Boddapati, F. Boekhout, J. Bommer, E. B. Hansen, T. Bosma, L. Bourdet, S. Boutin, P. Caroff, L. Casparis, M. Cassidy, A. W. Christensen, N. Clay, W. S. Cole, F. Corsetti, A. Cui, P. Dalampiras, A. Dokania, G. de Lange, M. de Moor, J. C. E. Saldaña, S. Fallahi, Z. H. Fathabad, J. Gamble, G. Gardner, D. Govender, F. Griggio, R. Grigoryan, S. Gronin, J. Gukelberger, S. Heedt, J. H. Zamorano, S. Ho, U. L. Holgaard, W. H. P. Nielsen, H. Ingerslev, P. J. Krogstrup, L. Johansson, J. Jones, R. Kallaher, F. Karimi, T. Karzig, C. King, M. E. Kloster, C. Knapp, D. Kocon, J. Koski, P. Kostamo, M. Kumar, T. Laeven, T. Larsen, K. Li, T. Lindemann, J. Love, R. Lutchyn, M. Manfra, E. Memisevic, C. Nayak, B. Nijholt, M. H. Madsen, S. Markussen, E. Martinez, R. McNeil, A. Mullally, J. Nielsen, A. Nurmohamed, E. O'Farrell, K. Otani, S. Pauka, K. Petersson, L. Petit, D. Pikulin, F. Preiss, M. Q. Perez, K. Rasmussen, M. Rajpalke, D. Razmadze, O. Reentila, D. Reilly, R. Rouse, I. Sadovskyy, L. Sainiemi, S. Schreppler, V. Sidorkin, A. Singh, S. Singh, S. Sinha, P. Sohr, T. Stankevič, L. Stek, H. Suominen, J. Suter, V. Svidenko, S. Teicher, M. Temuerhan, N. Thiyagarajah, R. Tholapi, M. Thomas, E. Toomey, S. Upadhyay, I. Urban, S. Vaitiekėnas, K. Van Hoogdalem, D. V. Viazmitinov, S. Waddy, D. Van Woerkom, D. Vogel, J. Watson, J. Weston, G. W. Winkler, C. K. Yang, S. Yau, D. Yi, E. Yucelen, A. Webster, R. Zeisel, and R. Zhao, [InAs-Al Hybrid Devices Passing the Topological Gap Protocol](#)

- (2022).
- [22] H. Bombin, Topological Order with a Twist: Ising Anyons from an Abelian Model, *Physical Review Letters* **105**, 030403 (2010).
- [23] T. I. Andersen, Y. D. Lensky, K. Kechedzhi, I. Drozdov, A. Bengtsson, S. Hong, A. Morvan, X. Mi, A. Opremcak, R. Acharya, R. Allen, M. Ansmann, F. Arute, K. Arya, A. Asfaw, J. Atalaya, R. Babbush, D. Bacon, J. C. Bardin, G. Bortoli, A. Bourassa, J. Bovaird, L. Brill, M. Broughton, B. B. Buckley, D. A. Buell, T. Burger, B. Burkett, N. Bushnell, Z. Chen, B. Chiaro, D. Chik, C. Chou, J. Cogan, R. Collins, P. Conner, W. Courtney, A. L. Crook, B. Curtin, D. M. Debroy, A. D. T. Barba, S. Demura, A. Dunsworth, D. Eppens, C. Erickson, L. Faoro, E. Farhi, R. Fatemi, V. S. Ferreira, L. F. Burgos, E. Forati, A. G. Fowler, B. Foxen, W. Giang, C. Gidney, D. Gilboa, M. Giustina, R. Gosula, A. G. Dau, J. A. Gross, S. Habegger, M. C. Hamilton, M. Hansen, M. P. Harrigan, S. D. Harrington, P. Heu, J. Hilton, M. R. Hoffmann, T. Huang, A. Huff, W. J. Huggins, L. B. Ioffe, S. V. Isakov, J. Iveland, E. Jeffrey, Z. Jiang, C. Jones, P. Juhas, D. Kafri, T. Khattar, M. Khezri, M. Kieferová, S. Kim, A. Kitaev, P. V. Klimov, A. R. Klots, A. N. Korotkov, F. Kostritsa, J. M. Kreikebaum, D. Landhuis, P. Laptev, K.-M. Lau, L. Laws, J. Lee, K. Lee, B. J. Lester, A. Lill, W. Liu, A. Locharla, E. Lucero, F. D. Malone, O. Martin, J. R. McClean, T. McCourt, M. McEwen, K. C. Miao, A. Mieszala, M. Mohseni, S. Montazeri, E. Mount, R. Movassagh, W. Mruczkiewicz, O. Naaman, M. Neeley, C. Neill, A. Nersisyan, M. Newman, J. H. Ng, A. Nguyen, M. Nguyen, M. Y. Niu, T. E. O'Brien, S. Omonije, A. Petukhov, R. Potter, L. P. Pryadko, C. Quintana, C. Rocque, N. C. Rubin, N. Saei, D. Sank, K. Sankaragomathi, K. J. Satzinger, H. F. Schurkus, C. Schuster, M. J. Shearn, A. Shorter, N. Shutty, V. Shvarts, J. Skrzynny, W. C. Smith, R. Somma, G. Sterling, D. Strain, M. Szalay, A. Torres, G. Vidal, B. Villalonga, C. V. Heidweiller, T. White, B. W. K. Woo, C. Xing, Z. J. Yao, P. Yeh, J. Yoo, G. Young, A. Zalcman, Y. Zhang, N. Zhu, N. Zorbrist, H. Neven, S. Boixo, A. Megrant, J. Kelly, Y. Chen, V. Smelyanskiy, E.-A. Kim, I. Aleiner, and P. Roushan, *Observation of non-Abelian exchange statistics on a superconducting processor* (2022).
- [24] S. Xu, Z.-Z. Sun, K. Wang, L. Xiang, Z. Bao, Z. Zhu, F. Shen, Z. Song, P. Zhang, W. Ren, X. Zhang, H. Dong, J. Deng, J. Chen, Y. Wu, Z. Tan, Y. Gao, F. Jin, X. Zhu, C. Zhang, N. Wang, Y. Zou, J. Zhong, A. Zhang, W. Li, W. Jiang, L.-W. Yu, Y. Yao, Z. Wang, H. Li, Q. Guo, C. Song, H. Wang, and D.-L. Deng, *Digital simulation of non-Abelian anyons with 68 programmable superconducting qubits* (2022).
- [25] S. X. Cui, S.-M. Hong, and Z. Wang, Universal quantum computation with weakly integral anyons, *Quantum Information Processing* **14**, 2687 (2015).
- [26] M. Barkeshli and J. D. Sau, *Physical Architecture for a Universal Topological Quantum Computer based on a Network of Majorana Nanowires* (2015).
- [27] M. Barkeshli, C.-M. Jian, and X.-L. Qi, Theory of defects in Abelian topological states, *Physical Review B* **88**, 235103 (2013).
- [28] M. Barkeshli, C.-M. Jian, and X.-L. Qi, Genons, twist defects, and projective non-Abelian braiding statistics, *Physical Review B* **87**, 045130 (2013).
- [29] I. Cong, M. Cheng, and Z. Wang, Universal Quantum Computation with Gapped Boundaries, *Physical Review Letters* **119**, 170504 (2017).
- [30] S. Bravyi, M. B. Hastings, and F. Verstraete, Lieb-robinson bounds and the generation of correlations and topological quantum order, *Phys. Rev. Lett.* **97**, 050401 (2006).
- [31] Y.-J. Liu, K. Shtengel, A. Smith, and F. Pollmann, Methods for simulating string-net states and anyons on a digital quantum computer, *PRX Quantum* **3**, 040315 (2022).
- [32] R. Raussendorf, S. Bravyi, and J. Harrington, Long-range quantum entanglement in noisy cluster states, *Phys. Rev. A* **71**, 062313 (2005).
- [33] A. Bolt, G. Duclos-Cianci, D. Poulin, and T. M. Stace, Foliated quantum error-correcting codes, *Phys. Rev. Lett.* **117**, 070501 (2016).
- [34] L. Piroli, G. Styliaris, and J. I. Cirac, Quantum circuits assisted by local operations and classical communication: Transformations and phases of matter, *Phys. Rev. Lett.* **127**, 220503 (2021).
- [35] N. Tantivasadakarn, A. Vishwanath, and R. Verresen, *A hierarchy of topological order from finite-depth unitaries, measurement and feedforward* (2022).
- [36] B. Shi, Seeing topological entanglement through the information convex, *Phys. Rev. Research* **1**, 033048 (2019).
- [37] N. Tantivasadakarn, R. Thorngren, A. Vishwanath, and R. Verresen, Long-range entanglement from measuring symmetry-protected topological phases (2022), [arXiv:2112.01519 \[cond-mat.str-el\]](https://arxiv.org/abs/2112.01519).
- [38] R. Verresen, N. Tantivasadakarn, and A. Vishwanath, Efficiently preparing schrödinger's cat, fractons and non-abelian topological order in quantum devices (2022), [arXiv:2112.03061 \[quant-ph\]](https://arxiv.org/abs/2112.03061).
- [39] S. Bravyi, I. Kim, A. Kliesch, and R. Koenig, Adaptive constant-depth circuits for manipulating non-abelian anyons, [arXiv preprint arXiv:2205.01933](https://arxiv.org/abs/2205.01933) (2022).
- [40] N. Tantivasadakarn, R. Verresen, and A. Vishwanath, *The Shortest Route to Non-Abelian Topological Order on a Quantum Processor* (2022).
- [41] B. Yoshida, Topological phases with generalized global symmetries, *Physical Review B* **93**, 155131 (2016).
- [42] A. C. Potter and R. Vasseur, Symmetry constraints on many-body localization, *Physical Review B* **94**, 224206 (2016).
- [43] T. Senthil, Symmetry-protected topological phases of quantum matter, *Annual Review of Condensed Matter Physics* **6**, 299 (2015).
- [44] H. J. Briegel and R. Raussendorf, Persistent entanglement in arrays of interacting particles, *Phys. Rev. Lett.* **86**, 910 (2001).
- [45] C. Wang and M. Levin, Topological invariants for gauge theories and symmetry-protected topological phases, *Physical Review B* **91**, 165119 (2015).
- [46] P. Putrov, J. Wang, and S.-T. Yau, Braiding statistics and link invariants of bosonic/fermionic topological quantum matter in 2+1 and 3+1 dimensions, *Annals of Physics* **384**, 254 (2017).
- [47] A. Kulkarni, M. Mignard, and P. Schauenburg, *A Topological Invariant for Modular Fusion Categories* (2021).
- [48] G. Dauphinais and D. Poulin, Fault-tolerant quantum error correction for non-abelian anyons, *Communications in Mathematical Physics* **355**, 519 (2017).
- [49] T.-C. Lu, L. A. Lessa, I. H. Kim, and T. H. Hsieh, Measurement as a shortcut to long-range entangled quantum

- matter, *PRX Quantum* **3**, 040337 (2022).
- [50] G.-Y. Zhu, N. Tantivasadakarn, A. Vishwanath, S. Trebst, and R. Verresen, Nishimori's cat: stable long-range entanglement from finite-depth unitaries and weak measurements (2022), [arXiv:2208.11136 \[quant-ph\]](#).
- [51] J. Y. Lee, W. Ji, Z. Bi, and M. P. A. Fisher, Decoding measurement-prepared quantum phases and transitions: from ising model to gauge theory, and beyond (2022), [arXiv:2208.11699 \[cond-mat.str-el\]](#).
- [52] T.-C. Lu, Z. Zhang, S. Vijay, and T. H. Hsieh, Mixed-state long-range order and criticality from measurement and feedback (2023), [arXiv:2303.15507 \[cond-mat.str-el\]](#).
- [53] C. Mochon, Anyon computers with smaller groups, *Physical Review A* **69**, 032306 (2004).
- [54] R. Dijkgraaf and E. Witten, Topological gauge theories and group cohomology, *Communications in Mathematical Physics* **129**, 393 (1990).
- [55] R. Dijkgraaf, V. Pasquier, and P. Roche, Quasi hope algebras, group cohomology and orbifold models, *Nuclear Physics B - Proceedings Supplements* **18**, 60 (1991).
- [56] Y. Hu, Y. Wan, and Y.-S. Wu, Twisted quantum double model of topological phases in two dimensions, *Physical Review B* **87**, 125114 (2013).
- [57] M. d. W. Propitius, *Topological interactions in broken gauge theories* (1995).
- [58] L. Lootens, B. Vancraeynest-De Cuiper, N. Schuch, and F. Verstraete, Mapping between Morita-equivalent string-net states with a constant depth quantum circuit, *Physical Review B* **105**, 085130 (2022).
- [59] X. Chen, Y.-M. Lu, and A. Vishwanath, Symmetry-protected topological phases from decorated domain walls, *Nature Communications* **5**, 3507 (2014).
- [60] A. Coste, T. Gannon, and P. Ruelle, Finite Group Modular Data, *Nuclear Physics B* **581**, 679 (2000).
- [61] E. Verlinde, Fusion rules and modular transformations in 2D conformal field theory, *Nuclear Physics B* **300**, 360 (1988).
- [62] S. Sivarajah, S. Dilkes, A. Cowtan, W. Simmons, A. Edgington, and R. Duncan, $t|ket\rangle$: A Retargetable Compiler for NISQ Devices, *Quantum Science and Technology* **6**, 014003 (2021).
- [63] M. Iqbal, N. Tantivasadakarn, R. Verresen, S. Campbell, J. Dreiling, C. Figgatt, J. Gaebler, J. Johansen, M. Mills, J. Pino, A. Ransford, M. Rowe, P. Siegfried, R. Stutz, M. Foss-Feig, A. Vishwanath, and H. Dreyer, *Supporting Data for experiment "D4H2"* (2023).

Appendix A: Methods

1. Proof of (5) and colour algebra

Here we prove the relationship (5) between the star and logical operators, reproduced here for convenience:

$$\prod_{s \in \text{red } \star} A_s = (-1)^{\frac{1-\mathcal{Z}_{GH}}{2} \frac{1-\mathcal{Z}_{BV}}{2}} \times (-1)^{\frac{1-\mathcal{Z}_{GV}}{2} \frac{1-\mathcal{Z}_{BH}}{2}} \quad (\text{A1})$$

For ease of notation, one of the three colours is singled out but it is understood that equivalent statements hold for all permutations of colours and directions. By linearity, it suffices to show that the equation holds for all computational basis states. Since we are working in the $B_t = 1$ subspace, strings of $|1\rangle$ s of a given color must form closed loops on the honeycomb superlattices of that color. These loops can either be contractible or wrap around the torus. Therefore e.g., \mathcal{Z}_{GH} acts on computational basis states by counting the parity of strings of $|1\rangle$ s on green qubits wrapping around the torus in the vertical direction. The operator $(1 - \mathcal{Z}_{GH})/2 \times (1 - \mathcal{Z}_{BV})/2$ projects into the space of computational basis states that have an odd number of blue strings in the horizontal and green strings in the vertical direction. In this space, there must be an odd number of stars where these strings cross (and these stars must necessarily be red). On the other hand, the product of CZ s within a red star is -1 if and only if the star is such a crossing star, as can be verified by considering rotations of Extended Data Figure 8. Going through the same argument for the other colours and torus directions concludes the proof.

Note that (5) implies the ‘‘color algebra’’ (that we note here for completeness)

$$\prod_{s \in \text{red } \star} A_s \mathcal{X}_{BH} = \mathcal{Z}_{GH} \mathcal{X}_{BH} \prod_{s \in \text{red } \star} A_s \quad (\text{A2})$$

which follows by using $\mathcal{Z}_{BH} \mathcal{X}_{BV} = -\mathcal{X}_{BV} \mathcal{Z}_{BH}$.

2. Uniqueness of the $\mathcal{Z} = 1$ state and Ground State Degeneracy

Here we show the uniqueness of the ground state of (1) in a given logical sector, and show that there are exactly 22 logical sectors that contain ground states. These proofs hold for tori of arbitrary sizes, not just the 3×3 -torus implemented in the experiment. All of the statements in this section hold within the $B_t = 1$ -subspace.

We start by fixing a logical sector through the specification of a set of $z_{cd} = \pm 1$. Denote the set of kagome stars on the lattice by S (in the experiment $|S| = 9$). Select one red (s_R), one green (s_G) and one blue star (s_B). A counting argument reveals that the subspace defined by

$$\left\{ \mathcal{Z}_{cd} = z_{cd}, B_t = 1, A_s = 1 \mid c \in \{R, G, B\}, d \in \{H, V\}, \forall t, s \in S \setminus \{s_R, s_G, s_B\} \right\} \quad (\text{A3})$$

has dimension one. There are 6 logical $z_{cd} \mathcal{Z}_{cd}$ stabilisers and $2|S|$ triangular stabilisers, $2|S| - 3$ of which are independent due to $\prod_t B_t = 1$ individually for each of the colors, leading to $2|S| + 3$ independent stabilisers that are diagonal in the computational basis. The independence of these diagonal stabilisers follows from the same argument as in the toric code (products of Z -plaquettes wrap around the torus an even number of times). The A_s operators are independent from the logical and triangle operators since any product that does not involve all A_s of a given color (including s_R , s_G or s_B) contains off-diagonal terms. Finally, the A_s are mutually independent. To see this, pick any state in the correct logical sector with $A_s = \pm 1$. Then, this state can be transformed into a state with any other pattern of $A_s = \pm 1$ by connecting the plaquettes which are to be toggled to s_R , s_G or s_B , (depending on their color) using strings of Z operators (similar to the cleanup step of the protocol in Fig. 3). These operations do not change the B_t and logical operators. Since we have found $3|S|$ independent stabilizers on $3|S|$ qubits (and they commute in the $B_t = +1$ space) the common $+1$ -eigenspace is exactly one-dimensional.

The state $|z_{cd}\rangle$ in this one-dimensional space can now either be a ground state or a state with energy 2, 4 or 6 above the ground state, depending on the value of A_{s_R} , A_{s_G} and A_{s_B} . Their values now simply follow from equation (5) since in the space defined above e.g.,

$$\begin{aligned} A_{s_R} &= \prod_{s \in \text{red } \star} A_s \\ &= (-1)^{\frac{1-\mathcal{Z}_{GH}}{2} \frac{1-\mathcal{Z}_{BV}}{2}} \times (-1)^{\frac{1-\mathcal{Z}_{GV}}{2} \frac{1-\mathcal{Z}_{BH}}{2}} \end{aligned} \quad (\text{A4})$$

Therefore, $\prod_{s \in \text{red} \star} A_s = \prod_{s \in \text{green} \star} A_s = \prod_{s \in \text{blue} \star} A_s = +1$ in the logical sectors with an even number of colour-pair crossings, which, for completeness, is the set

$$(\mathcal{Z}_{RH}, \mathcal{Z}_{GH}, \mathcal{Z}_{BH}, \mathcal{Z}_{RV}, \mathcal{Z}_{GV}, \mathcal{Z}_{BV}) \in \{000000, \\ 000001, 000010, 000011, 000100, 000101, 000110, 000111, \\ 001000, 010000, 011000, 100000, 101000, 110000, 111000, \\ 001001, 010010, 011011, 100100, 101101, 110110, 111111\}.$$

where, for readability, we have labeled such bit strings with the values of the projectors $(1 + \mathcal{Z})/2$ instead of \mathcal{Z} (i.e., 0 or 1 instead of ± 1).

In the absence of an analytic proof, the measurement-based protocol would also allow for an experimental detection of the ground state degeneracy. To this end, a random state is first prepared on all data qubits. In a second and third step the projections $\prod_t (1 + B_t)/2$ and $\prod_s (1 + A_s)/2$ are applied (in that order) via coupling to and measurement of ancillary qubits. Finally the logical \mathcal{Z} -operators are measured. Since, on average, random states have the same overlap with all ground state sectors, we expect each of the 22 ‘‘allowed’’ bitstrings to appear with probability $\sim (1 - \text{noise})/22$, while the 42 bitstrings ‘‘forbidden’’ bitstrings appear with much lower probability $\sim \text{noise}/42$. To produce initial random states, approximate circuits may be sufficient, for example random Clifford circuits, or even random one-qubit unitaries, which have been shown to lead to reasonable result in the context of random measurements for the determination of entanglement entropies.

3. Fidelity Lower Bound

Here, we show how to bound the fidelity per site from the experimentally measured correlation functions. Specifically we compute a lower bound on the the fidelity of the prepared state ρ with respect to the unique state that is the $+1$ eigenstate of the star, triangle and logical operators A_s , B_t and \mathcal{Z}_{cd} (Fig. 3). We introduce the projectors (not to be confused with the braiding operators in the Borromean interferometry experiment)

$$\begin{aligned} R &= \prod_{s \in \text{red} \star} \frac{1 + A_s}{2} \prod_{t \in \text{green} \triangleright} \frac{1 + B_t}{2} \prod_{t \in \text{blue} \triangleright} \frac{1 + B_t}{2} \frac{1 + \mathcal{Z}_{GH}}{2} \frac{1 + \mathcal{Z}_{GV}}{2} \\ G &= \prod_{s \in \text{green} \star} \frac{1 + A_s}{2} \prod_{t \in \text{blue} \triangleright} \frac{1 + B_t}{2} \prod_{t \in \text{red} \triangleright} \frac{1 + B_t}{2} \frac{1 + \mathcal{Z}_{BH}}{2} \frac{1 + \mathcal{Z}_{BV}}{2} \\ B &= \prod_{s \in \text{blue} \star} \frac{1 + A_s}{2} \prod_{t \in \text{red} \triangleright} \frac{1 + B_t}{2} \prod_{t \in \text{green} \triangleright} \frac{1 + B_t}{2} \frac{1 + \mathcal{Z}_{RH}}{2} \frac{1 + \mathcal{Z}_{RV}}{2}. \end{aligned} \quad (\text{A5})$$

Here, the products run over all stars of a given color except one (which can be chosen arbitrarily) and all triangles inscribed in the stars of that color, where across all three operators one arbitrary triangle can be excluded from each color. It follows that

$$[R, G] = [G, B] = [B, R] = 0 \quad (\text{A6})$$

$$|\psi_0\rangle \langle \psi_0| = RGB \quad (\text{A7})$$

We now seek to bound $\langle \psi_0 | \rho | \psi_0 \rangle$ by the measured expectation values $\langle R \rangle = \text{Tr} \rho R$, $\langle G \rangle$ and $\langle B \rangle$. Since R , G and B are commuting projectors, there exists a common orthonormal eigenbasis $|\psi_k^{rgb}\rangle$ with $r, g, b \in \{0, 1\}$ that fulfills

$$\begin{aligned} R |\psi_k^{rgb}\rangle &= r |\psi_k^{rgb}\rangle \\ G |\psi_k^{rgb}\rangle &= g |\psi_k^{rgb}\rangle \\ B |\psi_k^{rgb}\rangle &= b |\psi_k^{rgb}\rangle \end{aligned} \quad (\text{A8})$$

and k is a degeneracy label. Expanding the prepared state in this basis

$$\rho = \sum p_{r'g'b'k'}^{rgbk} |\psi_k^{rgb}\rangle \langle \psi_{k'}^{r'g'b'}| \quad (\text{A9})$$

defines the coefficients $p_{r'g'b'k'}^{rgbk}$. Let us also introduce shorthand notation

$$P^{rgb} := \sum_k p_{r'g'b'k'}^{rgbk} \quad (\text{A10})$$

for the sum of the diagonal elements of ρ in a given sector in the basis chosen above. In this notation, the ground state fidelity is simply $\langle \psi_0 | \rho | \psi_0 \rangle = P^{111}$. We then have

$$\langle R \rangle = P^{111} + P^{110} + P^{101} + P^{100} \quad (\text{A11a})$$

$$\langle G \rangle = P^{111} + P^{110} + P^{011} + P^{010} \quad (\text{A11b})$$

$$\langle B \rangle = P^{111} + P^{011} + P^{101} + P^{001} \quad (\text{A11c})$$

$$1 = P^{000} + P^{001} + P^{010} + P^{011} + P^{100} + P^{101} + P^{110} + P^{111} \quad (\text{A11d})$$

By considering (A11a)+(A11b)+(A11c)-2(A11d), we see that P^{111} is minimized if $P^{100} = P^{010} = P^{001} = P^{000} = 0$. In this case

$$P^{111} = \langle R \rangle + \langle G \rangle + \langle B \rangle - 2 \quad (\text{A12})$$

and this is the lower bound for the fidelity. We have measured

$$\begin{aligned} \langle R \rangle &= 0.90(1) \\ \langle G \rangle &= 0.85(1) \\ \langle B \rangle &= 0.89(1) \end{aligned} \quad (\text{A13})$$

leading to a lower bound on the global fidelity of the prepared state

$$\langle \psi_0 | \rho | \psi_0 \rangle \geq 0.65(2). \quad (\text{A14})$$

The fidelity per qubit is

$$\sqrt[27]{\langle \psi_0 | \rho | \psi_0 \rangle} \geq 0.984(1). \quad (\text{A15})$$

These measurements do not take into readout errors. If one wants to assess the quality of the prepared state rather than the combined quality of state preparation and measurements, one must take into account the expectation values of R , G and B after measurement error mitigation. Based on prior characterisation of the measurement error transition matrix in the device, $p(\text{measure } 0 | \text{qubit is } 1) = 2.37\text{e-}3$, $p(\text{measure } 1 | \text{qubit is } 0) = 0.82\text{e-}3$, and we have computed the corrected values by writing the raw probability distribution as a matrix product state of bond dimension n_{shots} and applying the transition matrix inverse on each site (see Extended Data Figure 9 for detailed comparison). In principle, this correction accounts for both state preparation and measurement (SPAM) error. In practice, however, measurement errors dominate state preparation errors in the device. We find

$$\begin{aligned} \langle R \rangle_{\text{SPAM error mitigated}} &= 0.94(1) \\ \langle G \rangle_{\text{SPAM error mitigated}} &= 0.89(1) \\ \langle B \rangle_{\text{SPAM error mitigated}} &= 0.93(1) \end{aligned} \quad (\text{A16})$$

We infer that the prepared state actually has a global fidelity of

$$\langle \psi_0 | \rho | \psi_0 \rangle_{\text{SPAM error mitigated}} \geq 0.75(2) \quad (\text{A17})$$

and a fidelity per qubit

$$\sqrt[27]{\langle \psi_0 | \rho | \psi_0 \rangle_{\text{SPAM error mitigated}}} \geq 0.990(1). \quad (\text{A18})$$

Using equation (A11), we can also bound the fidelity from above by noticing that

$$P^{111} \leq \min \{ \langle R \rangle, \langle G \rangle, \langle B \rangle \} \quad (\text{A19})$$

We thus find

$$\langle \psi_0 | \rho | \psi_0 \rangle \in [0.65(2), 0.85(2)] \quad (\text{A20})$$

$$\sqrt[27]{\langle \psi_0 | \rho | \psi_0 \rangle} \in [0.984(1), 0.9940(7)] \quad (\text{A21})$$

without SPAM error mitigation and

$$\langle \psi_0 | \rho | \psi_0 \rangle_{\text{SPAM error mitigated}} \in [0.75(2), 0.88(1)] \quad (\text{A22})$$

$$\sqrt[27]{\langle \psi_0 | \rho | \psi_0 \rangle_{\text{SPAM error mitigated}}} \in [0.990(1), 0.9955(6)] \quad (\text{A23})$$

with SPAM error mitigation. This is compatible with the fact that the state preparation protocol uses $3^{1/3}$ two-qubit gates per qubit with fidelity 99.8% ($99.8\%^{3.3} \approx 99.3\%$) and the fact that gate errors typically dominate errors arising from dephasing and measurement cross-talk in the trap.

4. Classification of the anyons

In the main text, the Hamiltonian corresponds to a gauged \mathbb{Z}_2^3 Symmetry-Protected Topological state [41] and therefore is in the same family of models as the twisted quantum double $\mathcal{D}^\alpha(\mathbb{Z}_2^3)$ [54–56]. This model exhibits the same topological order as that of the quantum double of $\mathcal{D}(D_4)$ [57, 58]. We elect to present the anyon content based on the twisted quantum double. A mapping relating the two conventions can be found in Extended Data Table II.

First, recall that in the usual toric code, anyons are generated by an Abelian charge e and an Abelian flux m where $e^2 = m^2 = 1$. Both anyons are bosons, but they have -1 mutual statistics. The bound state em is an Abelian fermion. For three copies, all anyons of the toric code are generated by e_C and m_C where $C \in \{R, G, B\}$ is a color index for each copy.

The 22 anyons of the twisted quantum double $\mathcal{D}^\alpha(\mathbb{Z}_2^3)$ can be labeled similar to that of three copies of the toric code. Instead, all fluxes are non-Abelian.

1. Eight Abelian bosons generated by e_R, e_G, e_B . Because they are Abelian, they obey the usual fusion rules i.e. $e_R \times e_G = e_{RG}$.
2. Three non-Abelian bosons m_R, m_G, m_B . They braid with the corresponding charge of the same color with a -1 phase. I.e., m_R braids non-trivially with e_R , but trivially with e_G and e_B .
3. Three non-Abelian fermions $f_R = m_R \times e_R$.
4. Three non-Abelian bosons m_{RG}, m_{GB}, m_{RB} . One can interpret these as fluxes that respond to two colors. That is m_{RG} braids with both e_R and e_G , but braids trivially with e_B .
5. Three non-Abelian fermions $f_{RG} = m_{RG} \times e_R = m_{RG} \times e_G$
6. A non-Abelian semion s_{RGB} , which is a flux that responds to three colors. That is, it braids with e_R, e_G , and e_B .
7. A non-Abelian antisemion $\bar{s}_{RGB} = s_{RBG} \times e_{RGB}$

We summarize all the remaining fusion rules (up to permutation of colors and fusion of Abelian charges) in Extended Data Table I. For example, by permuting colors, one can infer the fusion rule $m_G \times m_G = (1+e_R)(1+e_B)$ by permuting colors, and by the fusion rule $f_R \times m_G = e_R \times (m_R \times m_G) = e_R \times (m_{RG} + f_{RG}) = f_{RG} + m_{RG}$.

Next, we describe qualitatively why braiding m_G around m_B toggles the fusion outcome of each non-Abelian flux pair to e_R . The twisted quantum double realizes a gauged Symmetry-Protected Topological (SPT) phase given by the cocycle α . Such SPT phase can be realized using a decorated domain wall construction [41, 59]. Specifically, the SPT phase can be realized by a superposition of blue domain walls decorated by 1D cluster states, which itself forms a 1D SPT state under the red and green symmetries. After gauging the symmetry, the blue domain wall is allowed to end, forming the deconfined excitation m_B . Furthermore, because the domain wall was decorated with a cluster state, its end point m_B now carries a two-dimensional projective representation inherited from the end point of the cluster state, and therefore becomes a non-Abelian excitation due to this degeneracy.

The 1D cluster state protected by the red and green symmetries has the property that the ground state under antiperiodic boundary conditions of the green symmetry is odd under the red symmetry. Such a boundary condition can be enforced by introducing a single domain wall. Therefore, by braiding m_G around m_B , a green domain wall cuts through the string operator of m_B . Inheriting the property from the cluster state, the entire m_B string is now charged under the red gauge symmetry, which implies that fusing back the m_B pair will result in a red gauge charge, e_R . By an identical argument, fusing the pair of m_G back together will also result in e_R .

We now provide more technical details on the derivation of the data corresponding to the twisted quantum double [57]. Here, we consider the twisted quantum double $\mathcal{D}^\alpha(\mathbb{Z}_2^3)$, where $\alpha \in H^3(\mathbb{Z}_2^3, U(1))$ is a 3-cocycle. Conveniently, we represent the generators of the group $A = \mathbb{Z}_2^3$ by order two elements R, G, B . Thus, any group element $a \in A$ can be represented as $a = R^{\rho_a} G^{\gamma_a} B^{\beta_a}$ for $\rho_a, \gamma_a, \beta_a \in \{0, 1\}$.

For the twisted quantum double of an Abelian group A , an anyon can be labeled by a pair (a, σ) where $a \in A$ and σ is a choice of projective irreducible representation corresponding to a 2-cocycle ω_a . Such a representation Γ_a^σ satisfies

$$\Gamma_a^\sigma(b)\Gamma_a^\sigma(c) = \omega_a(b, c)\Gamma_a^\sigma(bc), \quad (\text{A24})$$

and the 2-cocycle ω_a is related to the input 3-cocycle α via

$$\omega_a(b, c) = \frac{\alpha(a, b, c)\alpha(b, c, a)}{\alpha(b, a, c)}. \quad (\text{A25})$$

In particular, our 3-cocycle of interest is given by

$$\alpha(a, b, c) = (-1)^{\rho_a \gamma_b \beta_c} \quad (\text{A26})$$

which implies that

$$\omega_a(b, c) = (-1)^{\rho_a \gamma_b \beta_c + \gamma_a \rho_b \beta_c + \beta_a \rho_b \gamma_c} \quad (\text{A27})$$

We now discuss the possible anyons for each choice of group element $a \in A$

1. $a = 1$ ($(\rho_a, \gamma_a, \beta_a) = (0, 0, 0)$). In this case, the 2-cocycle ω_a is trivial. Therefore, Γ_1^σ corresponds to (linear) irreducible representations of \mathbb{Z}_2^3 , which correspond exactly to the choice of an element in A . We can therefore label such choices as $\sigma \in A$. These correspond to the eight Abelian charges.
2. $a = R$ ($(\rho_a, \gamma_a, \beta_a) = (1, 0, 0)$). We find the 2-cocycle $\omega_R(b, c) = (-1)^{\gamma_b \beta_c}$. Eq. (A24) then implies that $\Gamma_R(G)$ and $\Gamma_R(B)$ anticommute. There are two possible choices of Γ_R , which we label by $\sigma = \pm$

$$\Gamma_R^\pm(R) = \pm I, \quad \Gamma_R^\pm(G) = X, \quad \Gamma_R^\pm(B) = Z, \quad (\text{A28})$$

where X, Y, Z are Pauli matrices and I is the 2×2 identity matrix. The two choices correspond to the non-Abelian flux m_R and f_R , respectively. Similarly, by permutation of colors, we can define m_G, f_G, m_B, f_B corresponding to the representation $\Gamma_G^+, \Gamma_G^-, \Gamma_B^+, \Gamma_B^-$, respectively where

$$\Gamma_G^\pm(R) = Z, \quad \Gamma_G^\pm(G) = \pm I, \quad \Gamma_G^\pm(B) = X, \quad (\text{A29})$$

$$\Gamma_B^\pm(R) = X, \quad \Gamma_B^\pm(G) = Z, \quad \Gamma_B^\pm(B) = \pm I. \quad (\text{A30})$$

3. $a = RG$ ($(\rho_a, \gamma_a, \beta_a) = (1, 1, 0)$). We find the 2-cocycle $c_{RG}(b, c) = (-1)^{\gamma_b \beta_c + \rho_b \beta_c}$, which means that $\{\Gamma_{RG}(R), \Gamma_{RG}(B)\} = \{\Gamma_{RG}(G), \Gamma_{rg}(B)\} = 0$. There are two inequivalent choices given by

$$\Gamma_{RG}^\pm(R) = \pm X, \quad \Gamma_{RG}^\pm(G) = X, \quad \Gamma_{RG}^\pm(B) = Z, \quad (\text{A31})$$

which correspond to m_{RG} and f_{RG} , respectively. Permuting the colors gives m_{GB}, f_{GB} and m_{RB}, f_{RB} .

4. $a = RGB$ ($(\rho_a, \gamma_a, \beta_a) = (1, 1, 1)$). We find the 2-cocycle $\omega_{RGB}(b, c) = (-1)^{\gamma_b \beta_c + \rho_b \beta_c + \rho_b \gamma_c}$, which means that all three pairs anticommute. There are two inequivalent choices given by

$$\Gamma_{RGB}^\pm(R) = \pm X, \quad \Gamma_{RGB}^\pm(G) = \pm Y, \quad \Gamma_{RGB}^\pm(B) = \pm Z, \quad (\text{A32})$$

which correspond to s_{RGB} and \bar{s}_{RGB} , respectively.

For an Abelian twisted quantum double, the S and T matrices can be computed via the formula [60]

$$S_{(a,\sigma),(b,\tau)} = \frac{1}{|A|} \chi_a^\sigma(b)^* \chi_b^\tau(a)^* \quad T_{(a,\sigma),(b,\tau)} = \delta_{a,b} \delta_{\sigma,\tau} \frac{\chi_a^\sigma(a)}{\chi_a^\sigma(1)} \quad (\text{A33})$$

where $\chi_a^\sigma = \text{Tr}[\Gamma_a^\sigma]$ is the character of the corresponding representation. In particular, we find that

$$8S_{(a,\sigma),(b,\tau)} = \begin{cases} 1 & ; a = b = 1, \\ 2 \times (-1)^{\rho_a \rho_\tau + \gamma_a \gamma_\tau + \beta_a \beta_\tau} & ; a = 1, b \neq 1, \\ 4 \times \delta_{a,b} (-1)^{\rho_a \gamma_a \beta_a + \sigma \tau} & ; a \neq 1, b \neq 1, \end{cases} \quad (\text{A34})$$

$$\text{diag } T_{(a,\sigma)} = \begin{cases} 1 & ; a = 1, \\ (-1)^\sigma \times i^{\rho_a \gamma_a \beta_a} & a \neq 1. \end{cases} \quad (\text{A35})$$

where we remind that $\sigma \in A$ when $a = 1$ and $\sigma = \pm 1$ for $a \neq 1$. For completion, the full matrices are

$$\text{diag } T = \begin{pmatrix} 1 & e_R & e_G & e_B & e_{RG} & e_{GB} & e_{RB} & e_{RGB} & m_R & f_R & m_G & f_G & m_B & f_B & m_{RG} & f_{RG} & m_{GB} & f_{GB} & m_{RB} & f_{RB} & s_{RGB} & \bar{s}_{RGB} \\ (1 & 1 & 1 & 1 & 1 & 1 & 1 & 1 & 1 & -1 & 1 & -1 & 1 & -1 & 1 & -1 & 1 & -1 & 1 & -1 & i & -i) \end{pmatrix} \quad (\text{A36})$$

$$S = \frac{1}{8} \begin{pmatrix} 1 & 1 & 1 & 1 & 1 & 1 & 1 & 1 & 2 & 2 & 2 & 2 & 2 & 2 & 2 & 2 & 2 & 2 & 2 & 2 \\ 1 & 1 & 1 & 1 & 1 & 1 & 1 & 1 & -2 & -2 & 2 & 2 & 2 & 2 & -2 & -2 & 2 & 2 & -2 & -2 \\ 1 & 1 & 1 & 1 & 1 & 1 & 1 & 1 & 2 & 2 & -2 & -2 & 2 & 2 & -2 & -2 & -2 & -2 & 2 & 2 \\ 1 & 1 & 1 & 1 & 1 & 1 & 1 & 1 & 2 & 2 & 2 & 2 & -2 & -2 & 2 & 2 & -2 & -2 & -2 & -2 \\ 1 & 1 & 1 & 1 & 1 & 1 & 1 & 1 & -2 & -2 & -2 & -2 & 2 & 2 & 2 & 2 & -2 & -2 & -2 & -2 \\ 1 & 1 & 1 & 1 & 1 & 1 & 1 & 1 & 2 & 2 & -2 & -2 & -2 & -2 & -2 & -2 & 2 & 2 & -2 & -2 \\ 1 & 1 & 1 & 1 & 1 & 1 & 1 & 1 & -2 & -2 & 2 & 2 & -2 & -2 & -2 & -2 & -2 & -2 & 2 & 2 \\ 1 & 1 & 1 & 1 & 1 & 1 & 1 & 1 & -2 & -2 & -2 & -2 & -2 & -2 & 2 & 2 & 2 & 2 & 2 & -2 \\ 2 & -2 & 2 & 2 & -2 & 2 & -2 & -2 & 4 & -4 & 0 & 0 & 0 & 0 & 0 & 0 & 0 & 0 & 0 & 0 \\ 2 & -2 & 2 & 2 & -2 & 2 & -2 & -2 & -4 & 4 & 0 & 0 & 0 & 0 & 0 & 0 & 0 & 0 & 0 & 0 \\ 2 & 2 & -2 & 2 & -2 & -2 & 2 & -2 & 0 & 0 & 4 & -4 & 0 & 0 & 0 & 0 & 0 & 0 & 0 & 0 \\ 2 & 2 & -2 & 2 & -2 & -2 & 2 & -2 & 0 & 0 & -4 & 4 & 0 & 0 & 0 & 0 & 0 & 0 & 0 & 0 \\ 2 & 2 & 2 & -2 & 2 & -2 & -2 & -2 & 0 & 0 & 0 & 0 & 4 & -4 & 0 & 0 & 0 & 0 & 0 & 0 \\ 2 & 2 & 2 & -2 & 2 & -2 & -2 & -2 & 0 & 0 & 0 & 0 & -4 & 4 & 0 & 0 & 0 & 0 & 0 & 0 \\ 2 & -2 & -2 & 2 & 2 & -2 & -2 & 2 & 0 & 0 & 0 & 0 & 0 & 4 & -4 & 0 & 0 & 0 & 0 & 0 \\ 2 & -2 & -2 & 2 & 2 & -2 & -2 & 2 & 0 & 0 & 0 & 0 & 0 & -4 & 4 & 0 & 0 & 0 & 0 & 0 \\ 2 & 2 & -2 & -2 & -2 & 2 & -2 & 2 & 0 & 0 & 0 & 0 & 0 & 0 & 0 & 4 & -4 & 0 & 0 & 0 \\ 2 & 2 & -2 & -2 & -2 & 2 & -2 & 2 & 0 & 0 & 0 & 0 & 0 & 0 & 0 & -4 & 4 & 0 & 0 & 0 \\ 2 & -2 & 2 & -2 & -2 & -2 & 2 & 2 & 0 & 0 & 0 & 0 & 0 & 0 & 0 & 0 & 4 & -4 & 0 & 0 \\ 2 & -2 & 2 & -2 & -2 & -2 & 2 & 2 & 0 & 0 & 0 & 0 & 0 & 0 & 0 & 0 & 0 & -4 & 4 & 0 \\ 2 & -2 & -2 & -2 & 2 & 2 & 2 & -2 & 0 & 0 & 0 & 0 & 0 & 0 & 0 & 0 & 0 & 0 & 0 & -4 \\ 2 & -2 & -2 & -2 & 2 & 2 & 2 & -2 & 0 & 0 & 0 & 0 & 0 & 0 & 0 & 0 & 0 & 0 & 4 & -4 \end{pmatrix} \quad (\text{A37})$$

Using the S-matrix above, the fusion rules in Table I can be derived using the Verlinde formula [61]

$$N_{IJ}^K = \sum_L \frac{S_{IL} S_{JL} S_{KL}^*}{S_{1L}} \quad (\text{A38})$$

where N_{IJ}^K are fusion multiplicities for the process $I \times J = \sum_K N_{IJ}^K K$, and I, J, K, L are anyons.

Next, let us demonstrate that by creating a pair of m_G and m_B anyons, braiding them and fusing each pair back together, we are left with two e_R 's as fusion outcomes. To be concrete, we will consider creating a pair of m_G at positions 1 and 2 and a pair of m_B at positions 3 and 4. We then perform a full braid of m_G at position 2 and m_B at position 3, before fusing each pair back together. Note that because each flux has quantum dimension 2, the internal state forms a qubit on which the representations Γ act on.

To create a pair of m_G fluxes, we must ensure that the state transforms under the trivial representation of $\Gamma_G^+ \otimes \Gamma_G^+$. From Eq. A29, we see that the symmetry action of red, green and blue on the two sites given by $Z_1 Z_2, I_1 I_2, X_1 X_2$, respectively. Therefore, the ‘‘singlet’’ state under this symmetry action is stabilized $Z_1 Z_2$ and $X_1 X_2$ (i.e. the Bell state $\frac{1}{\sqrt{2}}(|\uparrow_1 \uparrow_2\rangle + |\downarrow_1 \downarrow_2\rangle)$). Similarly, a pair of m_B anyons created from the vacuum is stabilized by $X_3 X_4$ and $Z_3 Z_4$.

In general, the full braid of an anyon (a, σ) around (b, τ) is given by the unitary operation $\Gamma^\sigma(b)_a \times \Gamma_\tau^\sigma(a)$. In this case, we have $(a, \sigma) = (G, +)$ and $(b, \tau) = (B, +)$. Therefore, the braiding operation on sites 2 and 3 is implemented via $\Gamma_G^+(B) \times \Gamma_B^+(G) = X_2 Z_3$. Thus, we see qualitatively that we are toggling the fusion channel space of the m_G pair by X , as described in the main text. To see this explicitly, conjugating the original stabilizers, we see that the state after the braiding is stabilized by $-Z_1 Z_2, X_1 X_2, Z_3 Z_4, -X_3 X_4$. In particular, the state satisfies $\Gamma_G^+(R)_1 \Gamma_G^+(R)_2 = Z_1 Z_2 = -1$, which means it is charged under the red symmetry action. This signifies that the fusion outcome of the two m_G anyons will result in e_R . Similarly, $\Gamma_B^+(R)_3 \Gamma_B^+(R)_4 = X_3 X_4 = -1$, implying that the two m_B anyons also fuse into e_R .

We can also demonstrate that the Borromean ring braiding of m_R, m_G and m_B results in a phase -1 . The Borromean ring braiding can be deformed topologically to the following process [45]

1. Create m_R, m_G, m_B pairs at sites 1 and 2, 3 and 4, 5 and 6, respectively.
2. Braid sites 2 and 4 followed by 2 and 6
3. Braid (in the reverse direction) sites 2 and 4 followed by 2 and 6
4. Fuse each flux pair.

Braiding sites 2 and 4 is realized by the operation $\Gamma_R^+(G)_2 \Gamma_G^+(R)_4 = X_2 Z_4$ while braiding sites 2 and 6 is realized by $\Gamma_R^+(B)_2 \Gamma_B^+(R)_6 = Z_2 X_6$. Therefore, the total braiding is realized by the operation

$$(Z_2 X_6)^{-1} (X_2 Z_4)^{-1} (Z_2 X_6) (X_2 Z_4) = -1 \quad (\text{A39})$$

5. Qubit Reuse and Circuit Optimization Techniques

Here we describe the steps we need to realize the D_4 topological order on the H2 trapped ion device. The construction requires a total of $27 + 3 = 30$ physical qubits to create 27-qubit states. During the procedure 9 ancillas need to be measured for a layer of feed-forward. It is crucial to reuse some of those ancilla qubits to fit the protocol into the maximal qubit capacity (32) of the device. We begin by rewriting Eq. (2) as

$$|\psi_0\rangle = \prod_v H_v \langle +|_P \prod_{\langle v,p\rangle} CZ_{v,p} \prod_{\langle p,\tilde{p},\tilde{\tilde{p}}\rangle} e^{\pm \frac{i\pi}{8} Z_p Z_{\tilde{p}} Z_{\tilde{\tilde{p}}}} |+\rangle_P |+\rangle_V, \quad (\text{A40})$$

where $|+\rangle_P = |+\rangle_P |+\rangle_P |+\rangle_P$ and $|+\rangle_V = |+\rangle_V |+\rangle_V |+\rangle_V$ denote plaquette and vertex qubits over the red, green and blue sublattices. Moreover, the product over CZ s also spans over three sublattices which can be decoupled, i.e.,

$$\prod_{\langle v,p\rangle} CZ_{v,p} = \prod_{\langle v,p\rangle} CZ_{v,p} \prod_{\langle v,p\rangle} CZ_{v,p} \prod_{\langle v,p\rangle} CZ_{v,p}.$$

We can rearrange Eq. (A40) as

$$|\psi_0\rangle = \prod_v H_v \langle +|_P \prod_{\langle v,p\rangle} CZ_{v,p} |+\rangle_V \underbrace{\langle +|_P \langle +|_P \prod_{\langle p,\tilde{p},\tilde{\tilde{p}}\rangle} e^{\pm \frac{i\pi}{8} Z_p Z_{\tilde{p}} Z_{\tilde{\tilde{p}}}} |+\rangle_P \left(\prod_{\langle v,p\rangle} CZ_{v,p} |+\rangle_P |+\rangle_V \right) \left(\prod_{\langle v,p\rangle} CZ_{v,p} |+\rangle_P |+\rangle_V \right)}_{\text{step 1}}. \quad (\text{A41})$$

The construction is divided into two steps. In step 1, we act on the vertex qubits of the green and blue sublattices only, and all the plaquette qubits of all three sublattices. In total, we use $(9 + 9) = 18$ vertex and $(3 + 3 + 3) = 9$ plaquette qubits during step 1. At the end of step 1, we measure $(3 + 3) = 6$ plaquette qubits of the green and blue sublattices. During step 2, we reuse the 6 measured qubits as vertex qubits of the red sublattice and act with CZ gates before also measuring the plaquette qubits of the red sublattice.

During step 1, we choose to first implement the CZ gates between the vertices and plaquette qubit. For a given color, we have $3 + 3 = 6$ CZ gates between 3 vertex and 2 plaquette qubits (e.g., we have 3 CZ s between v_1, v_2, v_3 , and p_1 , and 3 CZ s between the same vertices and p_2). Since CZ gates for the blue and green sublattices act on qubits in the $|+\rangle$ state, the action of the later 3 CZ gates can be implemented by a single two-qubit gate. This can be seen

by the state-vector identity for e.g., the blue sublattice,

The figure contains two quantum circuit diagrams, (A42) and (A43). Diagram (A42) shows a sequence of operations on 9 qubits. The left side shows a grid of CNOT gates between qubits labeled $|0\rangle_{p_1}$ to $|0\rangle_{v_9}$. The right side shows a more complex circuit with H gates and CNOT gates, separated by vertical dashed lines. Diagram (A43) shows a similar structure but with a different arrangement of gates and H gates.

Similar identities also holds for the green sublattice. This leads to a reduction from $3 \times 6 \times 2 = 36$ to $3 \times 4 \times 2 = 24$ two-qubit gates for the products of CZ on the blue and green sublattices.

The $\exp(\pm \frac{i\pi}{8} Z_p Z_{\tilde{p}} Z_{\bar{p}})$ gate that acts on 3 plaquette qubits of distinct colors is decomposed as

$$e^{\pm \frac{i\pi}{8} Z_p Z_{\tilde{p}} Z_{\bar{p}}} = \begin{array}{c} \tilde{p} \\ \oplus \\ \tilde{p} \\ \oplus \\ p \\ \exp(\pm \frac{i\pi}{8} Z_p Z_{\tilde{p}}) \end{array} \quad (\text{A43})$$

This decomposition uses the parametrised entangling gate $\text{ZZPhase}(\theta) = e^{-i\theta/2Z \otimes Z}$ which is the native entangling gate on the device. Without any optimization, we need $18 \times 3 = 54$ gates to realize the action of $\exp(\pm \frac{i\pi}{8} Z_p Z_{\tilde{p}} Z_{\bar{p}})$ gates. Since the order of qubits in (A43) does not matter, we notice that the stacked action of $\exp(+\frac{i\pi}{8} Z_0 Z_1 Z_2)$ and $\exp(-\frac{i\pi}{8} Z_1 Z_2 Z_3)$ requires not 6 but 4 two-qubit gates (Extended Data Fig. 7). By using this ‘squared’ implementation of the triangular $\exp(\pm \frac{i\pi}{8} Z_p Z_{\tilde{p}} Z_{\bar{p}})$ gates we reduce the number of two-qubits gates for this step from 54 to $9 \times 4 = 36$.

By using these circuit optimizations, we reduce the gate count to $18 + 12 + 12 = 42$ two qubit gates for the ‘ CZ -chains’ and 36 two-qubit gates for the $\exp(\pm \frac{i\pi}{8} Z_p Z_{\tilde{p}} Z_{\bar{p}})$ gates which give us a total of $42 + 36 = 78$ two-qubit gates.

We used TKET for compiling circuits into native gates [62]. The resulting circuit (for state preparation only) consisted of 165 one-qubit gates, 60 $\text{ZZMax} = e^{-i\pi/4Z \otimes Z}$ and 18 ZZPhase gates, while the depth of the native circuit is 56.

DATA AVAILABILITY

The numerical data that support the findings of this study are available from Zenodo repository 10.5281/zenodo.7848424 [63].

CODE AVAILABILITY

The code used for numerical simulations is available from from Zenodo repository 10.5281/zenodo.7848424 [63].

ACKNOWLEDGEMENTS

We thank the broader team at Quantinuum for discussions, feedback and encouragement, especially David Hayes, Konstantinos Mechanetzidis, Luuk Coopmans, Yuta Kikuchi, Patty Lee and Ilyas Khan. N.T. is supported by the Walter Burke Institute for Theoretical Physics at Caltech. RV is supported by the Harvard Quantum Initiative Postdoctoral Fellowship in Science and Engineering. AV and RV are supported by the Simons Collaboration on Ultra-Quantum Matter, which is a grant from the Simons Foundation (618615, A.V.). The experimental data in this work was produced by the Quantinuum H2 trapped ion quantum computer, powered by Honeywell.

AUTHOR CONTRIBUTIONS

M.I. wrote the code generating the circuits for all experiments. The experiment was built and carried out by S.L.C., J.M.D., C.F., J.P.G., J.J., M.M., S.A.M., J.M.P., A.R., M.R.,P.S. and R.P.S. The data analysis and interpretation was done by M.I., N.T, M.F., A.V, R.V. and H.D.. N.T., A.V. and R.V. contributed to the ideation, theory and experiment design, including the definition of the operators for anyon creation, movement and annihilation. H.D. drafted the initial manuscript, which was refined by contributions from all authors, especially M.I., N.T., R.V. and A.V.

COMPETING INTERESTS

H.D. is a shareholder of Quantinuum. All other authors declare no competing interests.

ADDITIONAL INFORMATION

Correspondence and requests for materials should be addressed to H.D.

Appendix B: Extended Data Figures and Tables

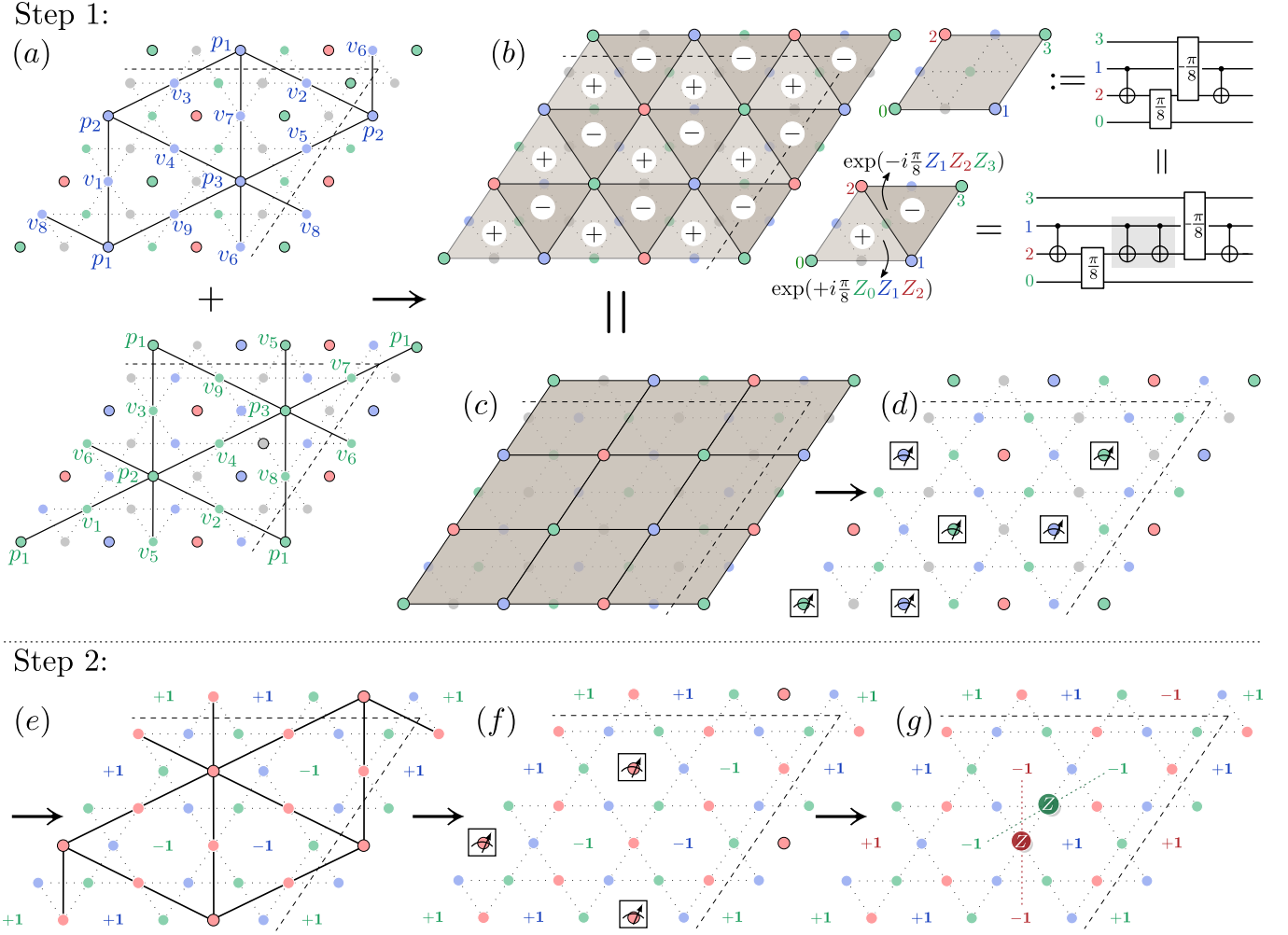


FIG. 7. More detail on the steps involved in preparing the ground state. In step 1a, we apply CZ gates on the blue and green sublattices, using the circuit optimisation techniques from section A 5. (b) shows the implementation of two adjacent $\exp(\pm \frac{i\pi}{8} Z_p Z_{\bar{p}} Z_{\bar{z}})$ gates within each square using 4 two-qubit gates. (c) as shown in (b), two adjacent $\exp(\pm \frac{i\pi}{8} Z_p Z_{\bar{p}} Z_{\bar{z}})$ gates within each square can be combined into one parallelogram of four two-qubit gates. (d) we measure the plaquette qubits of green and blue sublattices. In step 2e, we apply CZ gates between vertex and plaquette qubits of the red sublattice. (f) we measure plaquette qubits of the red sublattice. (g) shows a feed-forward action determined by the outcome of red, green and blue plaquette qubits.

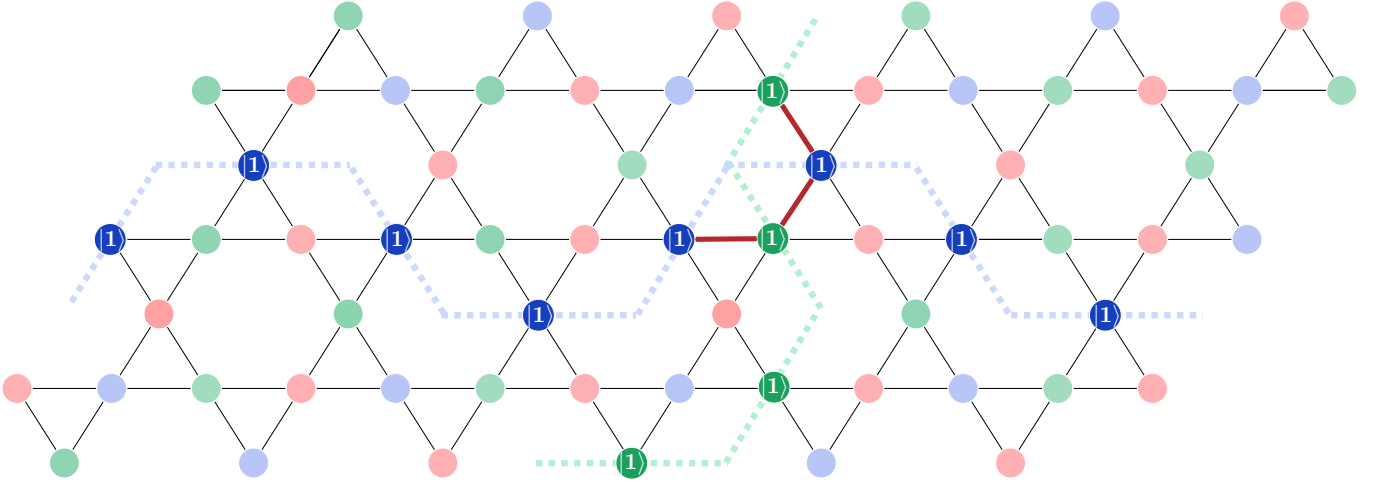


FIG. 8. **Evaluating the product $\prod_{s \in \text{red}} \star A_s$ for a computational basis state.** Shown is a computational basis state with an odd number of blue strings in the horizontal and green strings in the vertical direction on which $(1 - \mathcal{Z}_{GH})/2 \times (1 - \mathcal{Z}_{BV})/2 = +1$. There is an odd number of red stars (one) where these strings cross. By considering the 2^6 possible bitstrings around a hexagon, one can verify that $\prod CZ = -1$ around that hexagon if and only if the corresponding star is such a crossing star. Here, the only three CZ in the product $\prod_{s \in \text{red}} \star A_s$ which evaluate to -1 are marked with solid red lines.

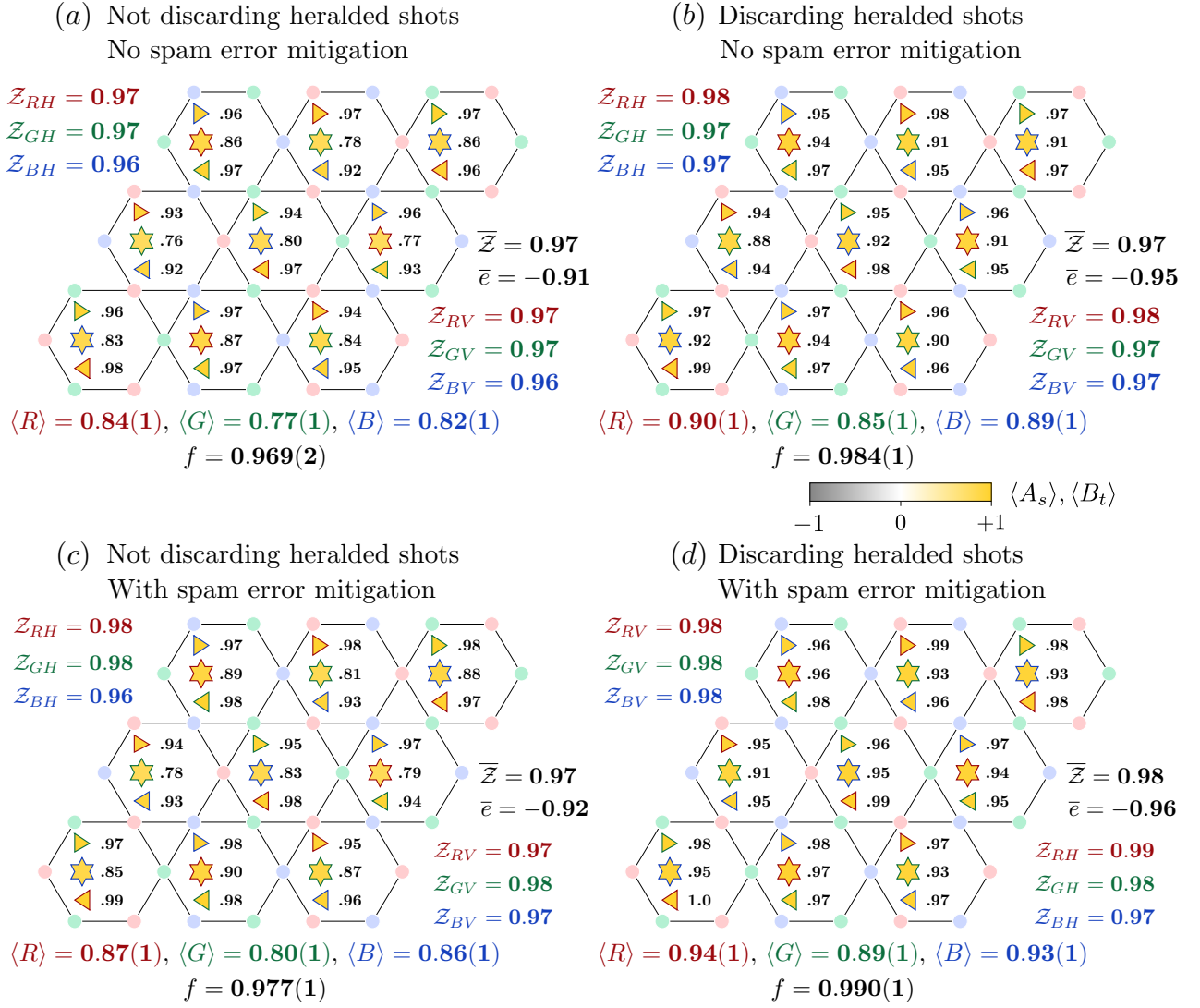


FIG. 9. **Effect of discarding heralded errors and measurement errors.** “Heralded shots” refers to the runs of the circuit where the measurement step in the ground state preparation protocol (Fig. 3c) reveals an odd number of Abelions due to noise. The spam error mitigation is described in section A 3. The average (maximal) standard error on the mean of the star and triangle operators in (a-d) is 0.014 (0.027). The average (maximal) standard error on logical operators in (a-d) is 0.007 (0.01). f denotes the lower bound on the resulting fidelity per qubit, calculated from R , G and B as defined in (A8). All main text figures correspond to the setting chosen in (b).

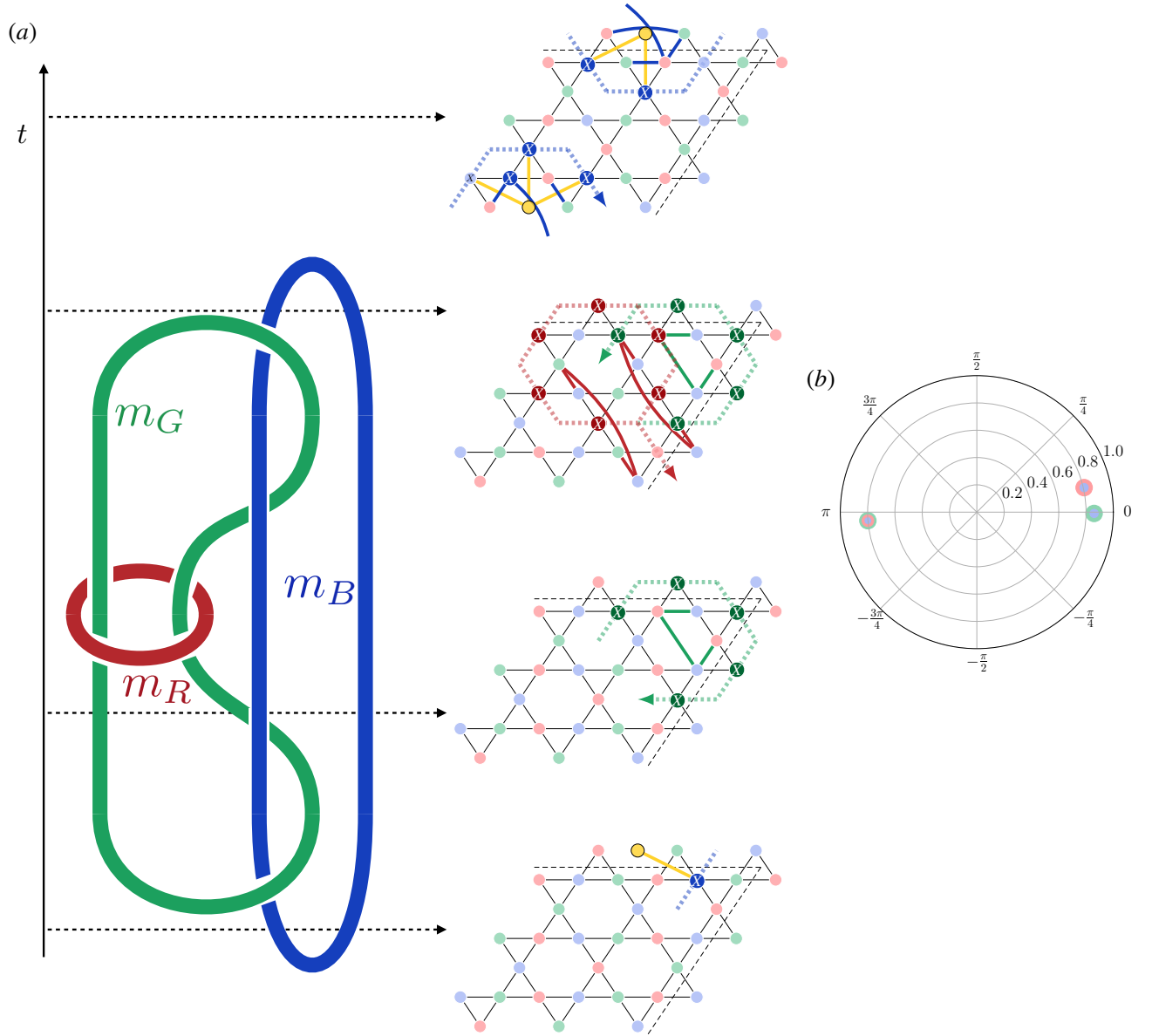


FIG. 10. **Details on the implementation of the Borromean Rings.** (a) Going up in time the thumbnails on the right show all gates applied during the braiding sequence of the Borromean rings (cf. section IV). The solid colored lines are CZ gates and the dashed black lines denote the periodic boundary conditions. The yellow ancilla qubit is controlling *all* blue gates including both X and CZ . After the ground state (2) is prepared, the ancilla is initialised and measured in the X - and Y -basis (in different shots) to extract both the real and the imaginary part of the phase. Since only the trajectory of the blue non-Abelian pair is controlled, this measures the phase of a spacetime diagram that is identical to the one shown on the left *plus* a disconnected diagram where the blue loop is missing. However, since the red and green loops in that disconnected part of the diagram are contractible, this is topologically equivalent to the Borromean Rings. (b) Measured value for the phase of the braid containing all three colors, as well as the braids where either red or green are removed. Writing $\langle \psi_0 | \text{braid} | \psi_0 \rangle = r e^{i\phi}$, the measured values for the different braids are: **red-green-blue**: $r = 0.80(2)$, $\phi = 1.02(2)\pi$, **red-blue**: $r = 0.81(2)$, $\phi = 0.07(2)\pi$, **green-blue**: $r = 0.86(2)$, $\phi = 2.00(2)\pi$. Uncertainty is one standard error on the mean.

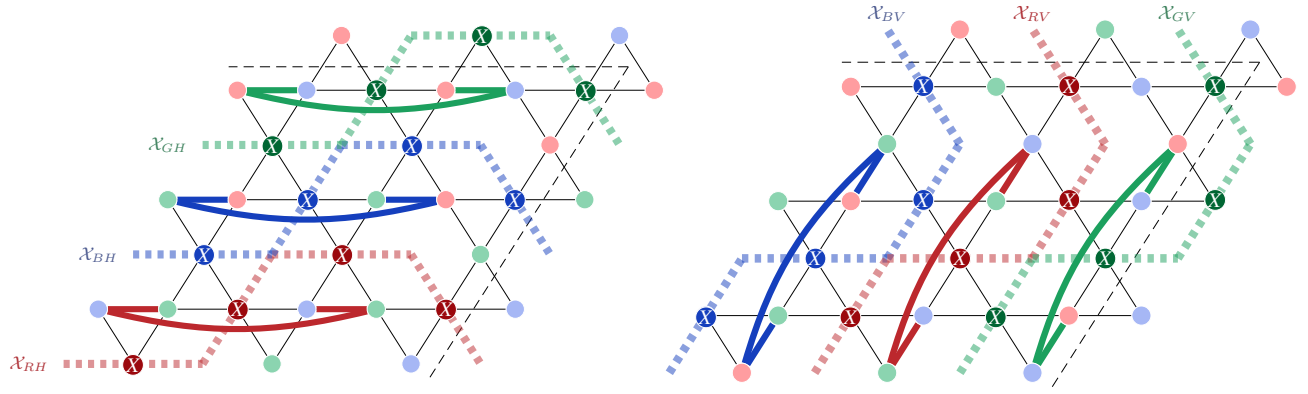


FIG. 11. **Non-contractible loops applied to switch logical sectors.** Operators applied to obtain all 22 ground states of the model in section V, specifically Fig. 6. Solid lines denote CZs, and dashed black lines denote the periodic boundary conditions. In the experiment, horizontal strings are applied before vertical strings. If one is interested in the highest possible fidelity state in a given sector, one may alternatively use the protocol (2) with a computational basis state in the desired sector.

	m_R	m_{RG}	s_{RGB}
e	$m_R \times e_R = f_R$ $m_R \times e_G = m_R \times e_B = m_R$	$m_{RG} \times e_R = m_{RG} \times e_G = f_{RG}$ $m_{RG} \times e_{RG} = m_{RG} \times e_B = m_{RG}$	$s_{RGB} \times e_R = s_{RGB} \times e_{RG} = \bar{s}_{RGB}$ $s_{RGB} \times e_{RG} = s_{RGB}$
m_R	$m_R \times m_R = (1 + e_G)(1 + e_B)$ $m_R \times m_G = m_{RG} + f_{RG}$	$m_{RG} \times m_G = m_R + f_R$ $m_{RG} \times m_B = s_{RGB} + \bar{s}_{RGB}$	$s_{RGB} \times m_R = m_{GB} + f_{GB}$
m_{RG}		$m_{RG} \times m_{RG} = (1 + e_{RG})(1 + e_B)$	$s_{RGB} \times m_{RG} = m_B + f_B$
s_{RGB}			$s_{RGB} \times s_{RGB} = 1 + e_{RG} + e_{GB} + e_{RB}$

TABLE I. Summary of fusion rules up to permutation of colors

$\mathcal{D}(D_4)$			$\mathcal{D}^\alpha(\mathbb{Z}_2^3)$	dim.	T
Conj. class	Centralizer	irrep			
1	D_4	$\mathbf{1}$	1	1	1
1	D_4	\mathbf{s}_1	e_{RG}	1	1
1	D_4	\mathbf{s}_2	e_R	1	1
1	D_4	\mathbf{s}_3	e_G	1	1
1	D_4	$\mathbf{2}$	m_B	2	1
r^2	D_4	$\mathbf{1}$	e_{RGB}	1	1
r^2	D_4	\mathbf{s}_1	e_B	1	1
r^2	D_4	\mathbf{s}_2	e_{GB}	1	1
r^2	D_4	\mathbf{s}_3	e_{RB}	1	1
r^2	D_4	$\mathbf{2}$	f_B	2	-1
r	\mathbb{Z}_4	$\mathbf{1}$	m_{RG}	2	1
r	\mathbb{Z}_4	ω	s_{RGB}	2	i
r	\mathbb{Z}_4	ω^2	f_{RG}	2	-1
r	\mathbb{Z}_4	$\bar{\omega}$	\bar{s}_{RGB}	2	$-i$
s	\mathbb{Z}_2^2	$\mathbf{1}$	m_{GB}	2	1
s	\mathbb{Z}_2^2	$(-1, 1)$	m_G	2	1
s	\mathbb{Z}_2^2	$(1, -1)$	f_G	2	-1
s	\mathbb{Z}_2^2	$(-1, -1)$	f_{GB}	2	-1
rs	\mathbb{Z}_2^2	$\mathbf{1}$	m_{RB}	2	1
rs	\mathbb{Z}_2^2	$(-1, 1)$	m_R	2	1
rs	\mathbb{Z}_2^2	$(1, -1)$	f_R	2	-1
rs	\mathbb{Z}_2^2	$(-1, -1)$	f_{RB}	2	-1

TABLE II. Equivalence between D_4 anyons and twisted \mathbb{Z}_2^3 anyons. Anyons of the D_4 quantum double model can be classified by a choice of conjugacy class and an irreducible representation of the corresponding centralizer. Here, the group D_4 is generated by group elements r and s , which satisfy $r^4 = s^2 = (rs)^2 = 1$.

Ground State	$[e_1^*, e_1^1, e_1^2], [e_2^*, e_2^1, e_2^2], \dots [e_9^*, e_9^1, e_9^2]$ $\mathcal{Z}_{RH}, \mathcal{Z}_{GH}, \mathcal{Z}_{BH}, \mathcal{Z}_{RV}, \mathcal{Z}_{GV}, \mathcal{Z}_{BV}$ $\mathcal{X}_{RH}, \mathcal{X}_{GH}, \mathcal{X}_{BH}, \mathcal{X}_{RV}, \mathcal{X}_{GV}, \mathcal{X}_{BV}$
1,1,1,1,1,1 $\bar{e} = -0.946(4)$ $\bar{l} = 0.974(1)$ $\bar{\mathcal{X}} = -0.01(1)$	[0.94(1), 0.95(1), 0.97(1)], [0.91(1), 0.979(9), 0.95(1)], [0.91(1), 0.97(1), 0.97(1)], [0.88(2), 0.94(1), 0.94(1)], [0.92(1), 0.95(1), 0.980(8)], [0.91(2), 0.96(1), 0.95(1)], [0.92(1), 0.97(1), 0.988(6)], [0.94(1), 0.97(1), 0.97(1)], [0.90(1), 0.96(1), 0.96(1)] 0.981(3), 0.975(4), 0.967(5), 0.978(4), 0.973(4), 0.970(5) 0.050(2), -0.010(2), -0.023(1), -0.016(2), -0.007(2), -0.029(1)
-1,1,1,1,1,1 $\bar{e} = -0.937(6)$ $\bar{l} = 0.965(3)$ $\bar{\mathcal{X}} = -0.05(2)$	[0.95(2), 0.97(1), 0.95(2)], [0.90(3), 0.96(2), 0.98(1)], [0.93(2), 0.98(1), 0.99(1)], [0.83(3), 0.97(1), 0.94(2)], [0.89(3), 0.95(2), 0.98(1)], [0.87(3), 0.91(2), 0.90(3)], [0.90(3), 0.94(2), 0.96(1)], [0.94(2), 0.93(2), 0.99(1)], [0.85(3), 0.97(1), 0.97(1)] -0.979(6), 0.964(8), 0.960(8), 0.973(7), 0.962(8), 0.954(8) -0.117(4), 0.078(2), 0.025(2), -0.213(4), -0.109(4), 0.065(4)
1,-1,1,1,1,1 $\bar{e} = -0.949(5)$ $\bar{l} = 0.976(2)$ $\bar{\mathcal{X}} = 0.03(2)$	[0.95(2), 0.98(1), 0.98(1)], [0.89(3), 0.98(1), 0.94(2)], [0.92(2), 0.99(1), 0.95(2)], [0.93(2), 0.99(1), 0.97(1)], [0.86(3), 0.95(2), 0.98(1)], [0.92(2), 0.96(2), 0.95(2)], [0.92(2), 0.98(1), 0.97(1)], [0.90(3), 0.95(2), 0.99(1)], [0.93(2), 0.97(1), 0.97(1)] 0.982(5), -0.979(5), 0.972(6), 0.977(6), 0.981(5), 0.964(8) 0.067(2), 0.007(5), 0.023(2), -0.056(4), 0.082(5), 0.072(4)
1,1,-1,1,1,1 $\bar{e} = -0.925(7)$ $\bar{l} = 0.965(3)$ $\bar{\mathcal{X}} = 0.02(2)$	[0.88(3), 0.96(2), 0.94(2)], [0.90(3), 0.97(1), 0.98(1)], [0.88(3), 0.92(2), 0.97(1)], [0.92(2), 0.98(1), 0.99(1)], [0.91(3), 0.92(2), 0.98(1)], [0.81(4), 0.87(3), 0.93(2)], [0.91(3), 0.94(2), 0.95(2)], [0.82(4), 0.91(2), 0.96(2)], [0.89(3), 0.97(1), 0.97(1)] 0.981(6), 0.960(8), -0.965(7), 0.981(5), 0.94(1), 0.961(7) -0.041(2), 0.009(2), 0.060(4), 0.016(4), 0.016(4), 0.064(4)
1,1,1,-1,1,1 $\bar{e} = -0.952(5)$ $\bar{l} = 0.974(2)$ $\bar{\mathcal{X}} = -0.01(2)$	[0.93(2), 0.97(1), 0.94(2)], [0.91(3), 0.95(2), 0.97(1)], [0.88(3), 0.99(1), 0.96(2)], [0.92(2), 0.96(2), 0.96(2)], [0.92(2), 0.93(2), 0.99(1)], [0.98(1), 0.97(1), 0.98(1)], [0.94(2), 0.94(2), 0.97(1)], [0.97(1), 0.93(2), 1.0], [0.90(3), 0.98(1), 0.99(1)] 0.976(6), 0.970(7), 0.975(6), -0.974(6), 0.970(7), 0.979(6) -0.067(5), -0.135(4), -0.066(4), 0.126(5), 0.050(2), 0.049(3)
1,1,1,1,-1,1 $\bar{e} = -0.956(5)$ $\bar{l} = 0.974(2)$ $\bar{\mathcal{X}} = 0.00(2)$	[0.92(2), 0.98(1), 0.99(1)], [0.96(2), 0.97(1), 0.98(1)], [0.93(2), 1.0, 0.94(2)], [0.96(2), 0.96(2), 0.87(3)], [0.92(2), 0.96(2), 1.0], [0.92(2), 0.98(1), 0.96(2)], [0.94(2), 0.97(1), 0.98(1)], [0.90(3), 0.95(2), 0.95(2)], [0.96(2), 1.0, 0.99(1)] 0.974(7), 0.982(5), 0.964(7), 0.985(5), -0.980(6), 0.962(8) -0.007(5), 0.203(5), -0.161(5), 0.051(2), -0.123(5), 0.045(3)
1,1,1,1,1,-1 $\bar{e} = -0.941(6)$ $\bar{l} = 0.976(2)$ $\bar{\mathcal{X}} = -0.01(2)$	[0.92(2), 0.96(2), 0.97(1)], [0.89(3), 0.97(1), 0.96(2)], [0.95(2), 0.97(1), 0.98(1)], [0.88(3), 0.97(1), 0.98(1)], [0.92(2), 0.96(2), 0.96(2)], [0.89(3), 0.92(2), 0.98(1)], [0.95(2), 0.96(2), 0.97(1)], [0.85(3), 0.93(2), 0.94(2)], [0.89(3), 0.96(2), 0.97(1)] 0.977(6), 0.974(6), 0.974(6), 0.975(7), 0.986(4), -0.972(6) 0.017(4), -0.037(4), 0.019(4), 0.049(2), -0.077(2), -0.040(4)
-1,-1,1,1,1,1 $\bar{e} = -0.934(6)$ $\bar{l} = 0.968(3)$ $\bar{\mathcal{X}} = 0.03(2)$	[0.89(3), 0.96(2), 0.93(2)], [0.87(3), 0.96(2), 0.96(2)], [0.83(4), 0.92(2), 0.92(2)], [0.91(3), 0.96(2), 0.98(1)], [0.86(3), 0.99(1), 0.93(2)], [0.97(1), 0.97(1), 0.94(2)], [0.86(3), 0.98(1), 0.99(1)], [0.86(3), 0.94(2), 0.98(1)], [0.93(2), 0.99(1), 0.96(2)] -0.961(9), -0.970(7), 0.969(7), 0.974(7), 0.962(7), 0.974(6) 0.039(2), 0.041(2), 0.024(2), -0.088(4), 0.103(4), 0.046(5)
1,-1,-1,1,1,1 $\bar{e} = -0.930(6)$ $\bar{l} = 0.967(3)$ $\bar{\mathcal{X}} = 0.03(2)$	[0.91(3), 0.98(1), 0.90(3)], [0.78(4), 0.95(2), 0.95(2)], [0.92(2), 0.98(1), 0.96(2)], [0.92(2), 0.96(2), 0.93(2)], [0.88(3), 0.90(3), 0.98(1)], [0.89(3), 0.96(2), 0.94(2)], [0.93(2), 0.99(1), 0.96(2)], [0.85(3), 0.98(1), 0.94(2)], [0.81(4), 0.99(1), 0.99(1)] 0.973(6), -0.957(8), -0.971(7), 0.975(6), 0.952(8), 0.973(7) -0.003(1), 0.052(2), 0.010(2), 0.021(4), -0.073(4), 0.162(4)
-1,1,-1,1,1,1 $\bar{e} = -0.928(7)$ $\bar{l} = 0.971(2)$ $\bar{\mathcal{X}} = 0.02(2)$	[0.83(3), 0.95(2), 0.91(2)], [0.93(2), 0.95(2), 0.99(1)], [0.88(3), 0.96(2), 0.98(1)], [0.92(2), 0.98(1), 0.97(1)], [0.89(3), 0.95(2), 0.99(1)], [0.86(3), 0.89(3), 0.94(2)], [0.86(3), 0.96(2), 0.98(1)], [0.84(3), 0.96(2), 0.95(2)], [0.87(3), 0.97(1), 0.94(2)] -0.981(5), 0.971(6), -0.965(7), 0.990(4), 0.961(8), 0.959(8) 0.047(2), -0.003(1), -0.005(2), 0.020(4), -0.048(4), 0.121(4)
1,1,1,-1,1,1 $\bar{e} = -0.927(7)$ $\bar{l} = 0.965(3)$ $\bar{\mathcal{X}} = -0.00(2)$	[0.83(3), 0.91(3), 0.92(2)], [0.84(4), 0.98(1), 0.95(2)], [0.91(3), 0.98(1), 0.95(2)], [0.86(3), 0.95(2), 0.96(2)], [0.91(3), 0.93(2), 0.99(1)], [0.85(3), 0.92(2), 0.93(2)], [0.94(2), 0.93(2), 0.99(1)], [0.88(3), 0.94(2), 0.99(1)], [0.92(2), 0.97(1), 0.96(2)] 0.977(6), 0.962(8), 0.959(8), -0.971(7), -0.955(9), 0.965(8) -0.094(4), 0.095(5), 0.023(5), -0.042(2), 0.016(2), -0.023(1)
1,1,1,1,-1,1 $\bar{e} = -0.919(7)$ $\bar{l} = 0.959(3)$ $\bar{\mathcal{X}} = 0.02(2)$	[0.87(3), 0.96(2), 0.93(2)], [0.80(4), 0.97(1), 0.87(3)], [0.85(3), 0.99(1), 0.94(2)], [0.86(3), 0.96(2), 0.95(2)], [0.80(4), 0.81(4), 0.98(1)], [0.82(4), 0.92(2), 0.96(2)], [0.95(2), 0.94(2), 0.99(1)], [0.91(3), 0.95(2), 0.99(1)], [0.90(3), 0.96(2), 1.0] 0.969(7), 0.94(1), 0.948(9), 0.978(6), -0.958(8), -0.958(8) 0.094(4), 0.007(4), 0.050(4), 0.054(1), -0.121(2), 0.029(2)
1,1,1,-1,1,-1 $\bar{e} = -0.940(7)$ $\bar{l} = 0.971(3)$ $\bar{\mathcal{X}} = -0.01(2)$	[0.95(2), 0.99(1), 0.95(2)], [0.91(2), 0.990(9), 0.97(1)], [0.85(3), 0.95(2), 0.97(1)], [0.92(2), 0.95(2), 0.97(1)], [0.87(3), 0.91(2), 0.98(1)], [0.94(2), 0.92(2), 0.97(1)], [0.90(3), 0.93(2), 0.99(1)], [0.89(3), 0.92(2), 0.93(2)], [0.93(2), 0.97(1), 0.97(1)] 0.975(7), 0.961(7), 0.966(8), -0.985(4), 0.973(7), -0.966(8) 0.074(4), -0.102(4), 0.052(4), 0.021(2), -0.056(1), -0.065(2)

Ground State	$[e_1^{\uparrow}, e_1^{\downarrow}, e_1^{\rightarrow}], [e_2^{\uparrow}, e_2^{\downarrow}, e_2^{\rightarrow}], \dots [e_9^{\uparrow}, e_9^{\downarrow}, e_9^{\rightarrow}]$
	$\mathcal{Z}_{RH}, \mathcal{Z}_{GH}, \mathcal{Z}_{BH}, \mathcal{Z}_{RV}, \mathcal{Z}_{GV}, \mathcal{Z}_{BV}$ $\mathcal{X}_{RH}, \mathcal{X}_{GH}, \mathcal{X}_{BH}, \mathcal{X}_{RV}, \mathcal{X}_{GV}, \mathcal{X}_{BV}$
$-1,1,1,-1,1,1$ $\bar{e} = -0.947(6)$ $\bar{l} = 0.974(2)$ $\bar{\mathcal{X}} = -0.00(2)$	$[0.85(3), 0.95(2), 0.92(2)], [0.90(3), 0.95(2), 0.96(2)], [0.91(2), 0.96(2), 0.99(1)], [0.94(2), 0.96(2), 0.96(2)], [0.93(2), 0.95(2), 0.99(1)],$ $[0.96(1), 0.96(1), 0.97(1)], [0.91(2), 1.0, 0.98(1)], [0.90(3), 0.97(1), 0.96(1)], [0.90(3), 0.97(1), 0.97(1)]$ $-0.976(6), 0.979(6), 0.970(8), -0.976(7), 0.972(6), 0.970(7)$ $-0.047(4), 0.069(2), 0.083(2), -0.057(4), -0.076(2), 0.012(2)$
$1,-1,1,1,-1,1$ $\bar{e} = -0.941(6)$ $\bar{l} = 0.967(3)$ $\bar{\mathcal{X}} = 0.05(2)$	$[0.87(3), 0.94(2), 0.91(2)], [0.89(3), 0.92(2), 0.90(3)], [0.89(3), 0.99(1), 0.96(2)], [0.92(2), 1.0, 0.93(2)], [0.94(2), 1.0, 0.99(1)],$ $[0.90(3), 0.93(2), 0.95(2)], [0.95(2), 0.99(1), 0.97(1)], [0.90(3), 0.94(2), 0.99(1)], [0.90(3), 0.99(1), 0.97(1)]$ $0.984(5), -0.968(8), 0.954(8), 0.975(6), -0.968(8), 0.951(9)$ $0.027(2), 0.053(5), 0.029(3), 0.034(2), 0.190(5), -0.029(2)$
$1,1,-1,1,1,-1$ $\bar{e} = -0.923(7)$ $\bar{l} = 0.963(3)$ $\bar{\mathcal{X}} = 0.04(2)$	$[0.96(2), 0.99(1), 0.97(1)], [0.80(4), 0.91(3), 0.96(2)], [0.91(3), 0.98(1), 0.94(2)], [0.83(4), 0.94(2), 0.99(1)], [0.89(3), 0.88(3), 0.97(1)],$ $[0.85(3), 0.96(2), 0.94(2)], [0.96(2), 0.97(1), 0.99(1)], [0.85(3), 0.93(2), 0.88(3)], [0.80(4), 0.93(2), 0.94(2)]$ $0.967(7), 0.951(9), -0.981(5), 0.95(1), 0.957(8), -0.970(7)$ $-0.002(2), 0.106(2), 0.053(5), 0.058(2), 0.095(3), -0.053(5)$
$-1,-1,-1,1,1,1$ $\bar{e} = -0.935(7)$ $\bar{l} = 0.972(2)$ $\bar{\mathcal{X}} = 0.01(2)$	$[0.85(3), 0.95(2), 0.91(2)], [0.84(4), 0.96(2), 0.92(2)], [0.93(2), 0.97(1), 0.97(1)], [0.83(4), 0.94(2), 0.96(2)], [0.95(2), 0.95(2), 0.97(1)],$ $[0.90(3), 0.95(2), 0.99(1)], [0.90(3), 0.98(1), 0.97(1)], [0.87(3), 0.96(2), 0.99(1)], [0.89(3), 0.99(1), 0.98(1)]$ $-0.971(7), -0.975(6), -0.971(7), 0.978(6), 0.972(6), 0.963(7)$ $0.012(1), 0.060(1), 0.012(1), -0.077(4), 0.041(5), -0.005(4)$
$1,1,1,-1,-1,-1$ $\bar{e} = -0.938(6)$ $\bar{l} = 0.970(2)$ $\bar{\mathcal{X}} = 0.00(2)$	$[0.92(2), 0.96(2), 0.97(1)], [0.93(2), 0.94(2), 0.98(1)], [0.84(3), 0.99(1), 0.96(2)], [0.96(2), 0.98(1), 0.98(1)], [0.89(3), 0.95(2), 0.96(2)],$ $[0.86(3), 0.96(2), 0.95(2)], [0.80(4), 0.91(3), 0.97(1)], [0.88(3), 0.97(1), 0.90(3)], [0.97(1), 0.99(1), 0.98(1)]$ $0.981(5), 0.952(8), 0.975(6), -0.974(7), -0.966(7), -0.973(6)$ $0.093(4), -0.003(5), -0.081(4), 0.061(1), -0.062(1), 0.021(1)$
$-1,-1,1,-1,-1,1$ $\bar{e} = -0.937(7)$ $\bar{l} = 0.974(2)$ $\bar{\mathcal{X}} = -0.01(2)$	$[0.86(3), 0.92(2), 0.92(2)], [0.87(3), 0.96(2), 0.94(2)], [0.87(3), 0.95(2), 0.97(1)], [0.92(2), 1.0, 0.93(2)], [0.90(3), 0.96(2), 0.98(1)],$ $[0.89(3), 0.94(2), 0.98(1)], [0.93(2), 0.98(1), 1.0], [0.92(2), 0.96(2), 0.99(1)], [0.88(3), 0.98(1), 0.93(2)]$ $-0.986(4), -0.981(6), 0.965(7), -0.988(4), -0.970(7), 0.956(8)$ $0.005(2), 0.012(2), -0.059(1), 0.058(2), -0.023(2), -0.073(1)$
$1,-1,-1,1,-1,-1$ $\bar{e} = -0.921(7)$ $\bar{l} = 0.966(3)$ $\bar{\mathcal{X}} = 0.00(2)$	$[0.83(4), 0.91(3), 0.98(1)], [0.93(2), 1.0, 0.94(2)], [0.88(3), 0.92(2), 0.99(1)], [0.88(3), 0.97(1), 0.94(2)], [0.75(4), 0.83(3), 0.95(2)],$ $[0.92(2), 0.94(2), 0.95(2)], [0.84(3), 0.94(2), 0.98(1)], [0.86(3), 0.96(2), 0.95(2)], [0.93(2), 0.99(1), 0.95(2)]$ $0.986(4), -0.948(9), -0.965(7), 0.984(5), -0.957(8), -0.953(8)$ $0.005(1), 0.035(2), -0.054(2), 0.044(1), 0.014(2), -0.036(2)$
$-1,-1,-1,1,-1,-1$ $\bar{e} = -0.907(8)$ $\bar{l} = 0.964(3)$ $\bar{\mathcal{X}} = 0.02(1)$	$[0.90(3), 0.94(2), 0.88(3)], [0.75(4), 0.95(2), 0.92(2)], [0.80(4), 0.89(3), 0.97(1)], [0.84(3), 0.97(1), 0.92(2)], [0.91(3), 0.89(3), 0.98(1)],$ $[0.87(3), 0.86(3), 0.92(2)], [0.84(3), 0.96(2), 1.0], [0.89(3), 0.96(1), 0.93(2)], [0.76(4), 1.0, 0.99(1)]$ $-0.988(4), 0.963(7), -0.959(8), -0.988(4), 0.93(1), -0.954(8)$ $0.053(2), 0.026(1), 0.135(2), 0.023(2), -0.043(1), -0.076(2)$
$-1,-1,-1,-1,-1,-1$ $\bar{e} = -0.863(9)$ $\bar{l} = 0.930(4)$ $\bar{\mathcal{X}} = 0.00(1)$	$[0.78(4), 0.85(3), 0.80(4)], [0.89(3), 0.99(1), 0.89(3)], [0.84(3), 0.90(3), 1.0], [0.89(3), 0.96(2), 0.84(4)], [0.78(4), 0.74(4), 0.98(1)],$ $[0.60(5), 0.76(4), 0.86(3)], [0.78(4), 0.95(2), 0.98(1)], [0.77(4), 0.94(2), 0.87(3)], [0.74(4), 0.96(2), 0.97(1)]$ $-0.986(4), -0.91(1), -0.92(1), -0.980(5), -0.89(1), -0.89(1)$ $0.038(1), 0.081(1), -0.108(1), 0.045(1), 0.005(1), -0.046(1)$

TABLE III. Expectation values of the local, Z - and X -logical stabilizers for the 22 ground states of D_4 Hamiltonian (1). $[e_i^{\uparrow}, e_i^{\downarrow}, e_i^{\rightarrow}]$ denotes the expectation values of 12-body A_s stabilizer (e_i^{\uparrow}), left- (e_i^{\downarrow}), and right-pointing (e_i^{\rightarrow}) B_t stabilizers. Plaquettes have been enumerated from left to right and top to bottom, and the order is given by index i . In the left column, we show the Z -logical signature ($\mathcal{Z}_{RH}, \mathcal{Z}_{GH}, \mathcal{Z}_{BH}, \mathcal{Z}_{RV}, \mathcal{Z}_{GV}, \mathcal{Z}_{BV}$) of the ground state, energy density (\bar{e}), value of logical pinning function (\bar{l}), and the mean value of X -logical stabilizers ($\bar{\mathcal{X}}$).